Effect of the angle of attack on flow around an elliptic cylinder near a moving wall

Jianxun Zhu (朱建勋),[1, a)] Lars Erik Holmedal,[1] and Cai Tian (田偲)[1]

1. Department of Marine Technology, Norwegian University of Science and Technology, 7052, Trondheim, Norway

(Dated: 11 March 2022)

The present work investigates the combined effect of the angle of attack *AOA* (the angle between the semi-major axis of the cylinder and the vertical axis), and the gap ratio G/D (where G represents the distance between the cylinder center and the moving wall, and D denotes the semi-major axis of the elliptic cylinder) on the flow around an elliptic cylinder near a moving wall. Here *AOA* covers $\pm 15^o$, $\pm 30^o$ and $\pm 45^o$ with G/D ranging from 0.6 to 2.5. The Reynolds number (based on the free-stream velocity and the semi-major axis) is fixed to 150. The resulting Kármán vortex street, the two-layered wake and the secondary vortex street have been investigated and visualized. The resulting patterns have been classified and mapped out in the (G/D, *AOA*)-space. At small gap ratios, a clockwise rotation of the cylinder (negative *AOA*) leads to stronger suppression effect between the moving wall and the backside of the cylinder. This results in more transitions between the different wake patterns than for the counterclockwise rotated cylinder (positive *AOA*). As the cylinder is more rotated either clockwise or counterclockwise, (i.e., as $|AOA|$ increases), the crest value of the drag coefficient decreases while the crest value of the lift coefficient first increases and then decreases for $G/D \geq 1.0$. For a given G/D, the time-averaged drag coefficient decreases with the increased rotation of the cylinder, except for an increase observed as *AOA* increases from 0^o to 15^o for $G/D \leq 0.9$. Moreover, the lift force is directed upwards and downwards for positive and negative *AOA*, respectively, and its magnitude decreases with increasing G/D when the cylinder is counterclockwise rotated, while it increases when the cylinder is clockwise rotated.

[a)]Corresponding author: jianxun.zhu@ntnu.no

I. INTRODUCTION

The wake behind an isolated circular cylinder has been widely investigated because of its vital importance in understanding vortex shedding in engineering applications such as marine risers, sub-sea cables and pipelines[1,2]. For Reynolds numbers (based on the free-stream velocity and the cylinder diameter) larger than about 47, the well-known Kármán vortex street is present. Cimbala, Nagib, and Roshko[3] reported that this vortex street exhibits a transition to a two-layered wake farther downstream, followed by a secondary vortex street with larger scales than the primary ones. Durgin and Karlsson[4] and Karasudani and Funakoshi[5] concluded that the first transition is due to the convection of the vorticity within the vortices, which leads to distortion and rotation of the vortices aligned with the stream-wise direction at some downstream location. The physical mechanism behind the second transition was first attributed to the hydrodynamic instability of the mean wake by Cimbala, Nagib, and Roshko[3] and then further identified as the convective instability of the mean wake by Kumar and Mittal[6].

Although less attention has been paid on the elliptic cylinder compared to the circular cylinder, the wake behind an isolated elliptic cylinder has been investigated due to its practical impact on submarines[7], bridge piers[8] and heat exchangers[9]. This flow depends on the Reynolds number Re (based on the free-stream velocity and the semi-major axis of the cylinder), the ratio (AR) of the semi-minor to semi-major axis length of the elliptic cylinder and the angle of attack AOA (defined by the angle between the semi-major axis and the vertical axis). Thompson *et al.*[10] conducted two-dimensional numerical simulations for flow around an isolated elliptic cylinder with $AOA = 0^o$ and $AR \in [0,1]$ (where $AR = 0$ and 1 represent a normal flat plate and a circular cylinder, respectively) for $Re \leq 200$. They found that an increase of Re (for a given AR) or a decrease of AR (for a given Re) can lead to the two-layered wake and the secondary vortex street moving upstream, i.e., towards the cylinder. Moreover, the secondary vortex street becomes more irregular with either increasing Re or decreasing AR. The effect of AOA on the wake structures was investigated numerically by Paul, Arul Prakash, and Vengadesan[11] for $AR \in [0.1, 1.0]$ and for $Re \in [50, 200]$. It should be noted that AOA is defined by the angle between the inlet flow condition and the semi-major axis in their work, but here we use the present definition, i.e., the angle between the semi-major axis and the vertical axis. With this definition, for $AOA \in [45^o, 60^o]$, the wake consists of the Kármán vortex street only while a decrease of AOA from 45^o to 0^o (for given Re and AR) enhances the wake instability, leading to a higher vortex shedding frequency and the onset of the two-layered wake as well as the secondary vortex street. They also found that as AOA decreases from 60^o to 0^o (for given Re and AR) the time-averaged lift coefficient decreases while the time-averaged drag coefficient increases except for a drag reduction observed at $AOA = 0^o$ for $AR \in [0.4, 0.8]$. Qualitatively similar results were also observed by Shi, Alam, and Bai[12], who conducted two-dimensional numerical simulations for $AR \in [0.25, 1.0]$ and $AOA \in [0, 90^o]$ at $Re = 150$.

The near-wall effect on a circular cylinder translating above a plane wall in calm water have been investigated extensively using both the experimental measurements[13–15] and numerical simulations[16–18]. Here the flow depends on the Reynolds number Re and the gap ratio G/D (where G is the distance between the cylinder bottom and the bottom wall and D is the cylinder diameter). Huang and Sung[16] conducted two-dimensional simulations for flow around a circular

cylinder near a moving wall, finding a critical value $(G/D)_c = 0.28$ for $Re = 300$, below which the flow exhibits a transition from Kármán vortex shedding to a pair-wise vortex shedding where the vortex shed from the bottom part of the cylinder follows immediately the vortex shed from the top of the cylinder. This critical value decreases to about 0.25 as Re increases up to 500. As G/D decreases to 0.1 (for $Re = 300$), the vortex shed from the cylinder top dominates the wake flow, forming a single vortex row behind the cylinder while vortex shedding was not observed behind the bottom of the cylinder. These results coincide with the experimental findings of Taneda[13]. Huang and Sung[16] also found that the time-averaged lift coefficient decreases with increasing G/D while the time-averaged drag coefficient first increases as G/D increases up to a critical value $(G/D)_c$, and then decreases with a further increase of G/D. Moreover, they showed that *i*) for $G/D > 0.6$, an acceleration of the gap flow caused by a decrease of G/D enhances the vortex shedding frequency; *ii*) for $(G/D)_c < G/D < 0.6$, the vortex shedding frequency decreases rapidly due to the wall suppression effect; *iii*) for $G/D < (G/D)_c$, the vortex shedding frequency decreases slowly since the wake pattern exhibits a transition from Kármán vortex shedding to pair-wise vortex shedding. A comprehensive numerical investigation for $Re \leq 300$ and $G/D \in [0.1, 19.5]$ was conducted by Jiang *et al.*[18], showing that a decrease of G/D results in a stronger wall suppression effect, which leads to a larger critical Re for the onset of the vortex shedding.

Less attention has been paid to the flow around an elliptic cylinder translating above a plane wall. This is important for understanding the basic mechanisms for flow over small-scale and low-speed underwater robots with an elliptic cross section moving near the seabed[19,20], non-spherical particles[21] such as fish larvae moving near the seabed as well as other biological flows[22]. Moreover, this flow configuration can be used to investigate the effect of gap ratio on the transition from the Kármán vortex street to the two-layered wake and the transition from the two-layered wake to the secondary vortex street which do not occur for a circular cylinder translating above a plane wall at the same Re range[18]. Four wake patterns have been classified by Zhu *et al.*[23] for flow around an elliptic cylinder with $AR = 0.4$ and $AOA = 0^o$ near a moving wall for $Re \leq 150$ with $G/D \in [0.1, 5]$; *i*) at relatively large G/D, the flow, which is denoted as wake pattern A, contains the Kármán vortex street, the two-layered wake and the secondary vortex street; *ii*) a decrease of G/D suppresses the secondary vortex street, forming the wake pattern B; *iii*) a further decrease in G/D leads to the break-down of the Kármán vortex, resulting in a pair-wise vortex shedding (denoted wake pattern C) or *iv*) forming a quasi-steady near-wake region (with time-independent lift and drag coefficients) and a pair-wise vortex shedding farther downstream (denoted wake pattern D). They also found that the critical Re for the transition between the different wake patterns increases as G/D increases. An overall increase of the time-averaged drag coefficient with an increase of G/D is observed. Moreover, as G/D increases (for a given Re), the onset location of the two-layered wake (i.e., the distance to the cylinder center) first decreases due to a decrease in the gap flow velocity and then increases due to the weakening of the wall suppression effect.

The contribution from the present work can be viewed in the following context: First the flow over a circular cylinder near a moving wall was investigated by, e.g., Huang and Sung[16], Rao *et al.*[17] and Jiang *et al.*[18]. Since cylinders not necessarily circular, as outlined in the previous paragraph, these works were extended by Zhu *et al.*[23] to include flow over an elliptic cylinder near a moving wall. This extension is significant since both the wake and the hydrodynamic forces on the elliptic cylinder are substantially different from those for the circular cylinder. In the present

work, the flow over an elliptic cylinder near a moving wall, where the cylinder is rotated relative to the vertical axis, is investigated. Since the angle of attack (AOA) plays a key role in the transition between wake patterns as well as the hydrodynamic forces on the elliptic cylinder, it is important to investigate the combined effect of AOA and G/D where G here is the distance between the cylinder center and the moving wall. Moreover, taking the AOA into account mimics the flow over an elliptic cylinder moving over a sloping bottom. The purpose of the present work is thus to investigate how the flow is affected by rotation (i.e., AOA) of the elliptic cylinder near a moving wall. Specifically, we consider an elliptic cylinder with $AR = 0.4$ at $Re = 150$ for $G/D \in [0.6, 2.5]$. A detailed analysis of the effect of AOA on the vortex shedding, the wake as well as the lift and drag coefficients for different gap ratios is presented.

II. PROBLEM DEFINITION AND GOVERNING EQUATIONS

The current paper addresses the flow over an inclined elliptic cylinder near a moving wall as shown in figure 1. The aspect ratio of the elliptic cylinder equals to 0.4, given by the minor (a) to major (D) axis length ratio, i.e., $AR = a/D$. The gap ratio is given by G/D, and the Reynolds number is based on the semi-major axis, i.e. $Re = UD/\upsilon$ where υ is the kinematic viscosity. The angle of attack (AOA) is given by the angle between the semi-major axis and the vertical axis (red dashed line). The clockwise and counterclockwise rotations of the semi-major axis away from the vertical axis are denoted as negative and positive AOA, respectively; $AOA = 0^o$ when the semi-major axis coincide with the vertical axis. Here the incompressible flow with a constant density ρ is governed by the dimensionless two-dimensional Navier-Stokes equations given as

$$\frac{\partial u_i}{\partial x_i} = 0 \tag{1}$$

$$\frac{\partial u_i}{\partial t} + \frac{\partial u_i u_j}{\partial x_j} = -\frac{\partial p}{\partial x_i} + \frac{1}{Re}\frac{\partial^2 u_i}{\partial x_j \partial x_j} \tag{2}$$

where the Einstein notation using repeated indices is applied. Here $u_i = (u,v)$ and $x_i = (x, y)$ for $i = 1$ and 2, indicate the velocity and Cartesian coordinates, respectively, whilst t and p denote the time and pressure, respectively. The velocity, time, pressure and length are scaled by U, D/U, ρU^2 and D, respectively.

III. NUMERICAL METHODS

A projection method is used for solving the Navier-Stokes equations. The convective terms are discretized by a second order Adams–Bashforth scheme while the diffusive terms are discretized using the Crank-Nicolson scheme. The spatial derivatives are discretized with a second-order centred finite difference scheme on a staggered grid arrangement. The Poisson equation for pressure correction is solved using a biconjugate gradient stabilized method (BiCGSTAB) with a SIP (Strongly Implicit procedure) preconditioner. The cylinder geometry is taken into account by a direct-forcing immersed boundary method, which is described in detail in Zhu *et al.*[23].

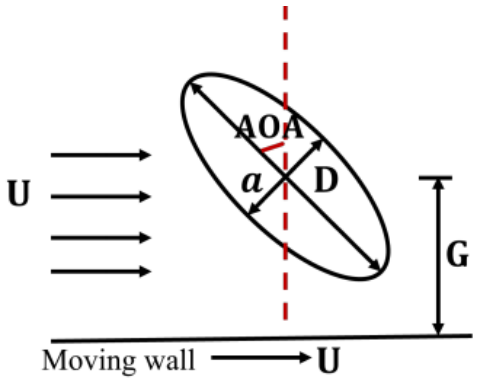

FIG. 1. Sketch of the flow over an inclined elliptic cylinder near a moving wall.

IV. MESH CONVERGENCE STUDY

The code applied in this work has been validated in previous works[23,24] for flow around an isolated elliptic and circular cylinders for Reynolds numbers up to 200. In this work, numerical simulations of flow over an elliptic cylinder with $AOA \in [-45^o, 45^o]$ near a moving wall have been conducted for $G/D \in [0.6, 2.5]$ at $Re = 150$. Figure 2 shows the computational domain and boundary conditions in the present work. The inlet and outlet are located at $20D$ and $50D$ away from the cylinder center, respectively. The distance between the top and the bottom wall is $20D$ while the bottom wall is located at the gap distance (G) from the cylinder center. A dimensionless constant velocity $u = 1$ is applied at the inlet and the bottom wall is also moving with the velocity $u = 1$. A Neumann condition is applied for the velocity at the top and outlet boundaries. A no-slip condition is imposed at the cylinder surface and the bottom wall, which moves towards the right. The pressure at the outlet is set to be zero while a Neumann condition is applied for the pressure correction at other boundaries.

It should be noted that if the flow (in the absence of the cylinder) is driven by an infinite long plate with a constant velocity U_0, then this flow configuration exhibits an analytically transient solution[25] given by $u/U_0 = 1 - erf(y/\sqrt{\upsilon t})$, where $erf(k)$ denotes a complementary error function, which approaches zero as k approaches zero, implying that u approaches U_0 as the flow becomes steady, i.e., the quiescent flow evolves to uniform flow with a constant velocity U_0.

A uniform grid ($\Delta x = \Delta y$) is applied to the square region (marked by a blue box in figure 2) around the cylinder. The left, right and top edges of this region are located at a distance of $0.8D$ from the cylinder center; the corresponding bottom edge is located at the distance G away from the cylinder. The grid is stretched from the top, left, and right edges of this region towards the top, inlet and outlet of the computational domain using constant geometric stretch ratios less than 1.05.

A mesh convergence study was conducted for the flow over an elliptic cylinder with $AOA \in [15^o, 45^o]$ near a moving wall for $G/D = 0.6$ at $Re = 150$ using three different grid resolutions. Table I shows the comparison of the Strouhal number $St = fD/U$ (where f denotes the vortex shedding frequency), the time-averaged drag coefficient $\overline{C_D} = \frac{1}{N}\sum_{i=1}^{N} \frac{2F_D(t)}{\rho U^2 D^2}$ (where F_D represents the drag force on the cylinder while N indicates the number of values in the time history for

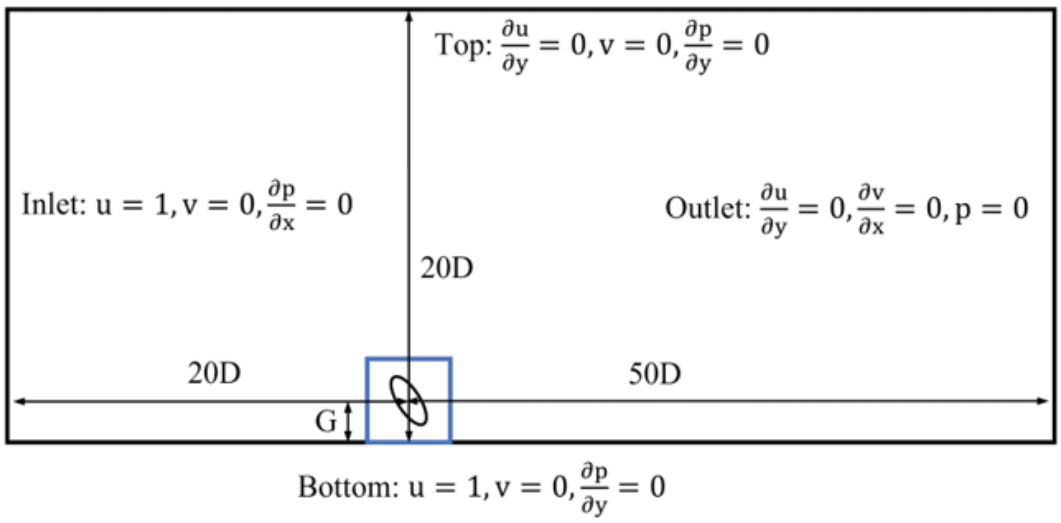

FIG. 2. Computational domain and boundary conditions of the flow around an inclined elliptic cylinder near a moving wall.

statistics) and the time-averaged lift coefficient $\overline{C_L} = \frac{1}{N}\sum_{i=1}^{N} \frac{2F_L(t)}{\rho U^2 D^2}$ (where F_L represents the lift force on the cylinder) obtained from the coarse ($\Delta x = \Delta y = 0.02$), standard ($\Delta x = \Delta y = 0.015$) and fine ($\Delta x = \Delta y = 0.01$) grid resolutions.

The results obtained from the standard grid resolution deviate less than 1% from those obtained from the fine grid resolution. Hence, the standard grid resolution is used in the present study. Here the grid is stretched from the left and right edges of the uniform-mesh region to the inlet and outlet, respectively, (with the grid size Δx ranging from 0.015 to 0.2) as well as from the top edge to the top boundary (with the grid size Δy ranging from 0.015 to 1.5). Here the stretch ratio is less than 1.05, and the time step size is fixed to 0.002 for all simulations to ensure the CFL (Courant-Friedrichs-Lewy) number smaller than 0.5.

V. RESULTS AND DISCUSSION

A. Wake patterns

Numerical simulations of flow around an elliptic cylinder with $AOA \in [-45^o, 45^o]$ near a moving wall have been conducted for $G/D \in [0.6, 2.5]$. The Reynolds number Re here is fixed to 150 where the secondary vortex street can be clearly observed at G/D=2.5. Hence, we can investigate the effect of AOA on the secondary vortex street. The combined effect of the Re and G/D has been investigated for a fixed $AOA = 0^o$ by Zhu *et al.*[23], finding that an increase of Re can lead to a transition sequence of steady flow -> wake pattern D -> wake pattern C -> wake pattern B -> wake pattern A; these wake patterns will be further described below. In the present work, we found that the change of AOA does not generate new wake patterns but changes the critical G/D and Re for the transition between different wake patterns. Hence, the effect of Re for given AOA and G/D on the transition between different wake patterns remains qualitatively similar as that observed by

Mesh	AOA	St	$\overline{C}_D$	$\overline{C}_L$
Coarse ($\Delta x = \Delta y = 0.02$)	15^o	0.113	1.686	0.697
Standard ($\Delta x = \Delta y = 0.015$)	15^o	0.113	1.694	0.685
Fine ($\Delta x = \Delta y = 0.01$)	15^o	0.113	1.708	0.686
Relative error (%)	-	0	0.82	0.14
Coarse ($\Delta x = \Delta y = 0.02$)	30^o	0.137	1.610	0.958
Standard ($\Delta x = \Delta y = 0.015$)	30^o	0.137	1.612	0.939
Fine ($\Delta x = \Delta y = 0.01$)	30^o	0.137	1.623	0.945
Relative error (%)	-	0	0.67	0.63
Coarse ($\Delta x = \Delta y = 0.02$)	45^o	0.18	1.349	1.012
Standard ($\Delta x = \Delta y = 0.015$)	45^o	0.177	1.312	1.045
Fine ($\Delta x = \Delta y = 0.01$)	45^o	0.177	1.322	1.05
Relative error (%)	-	0	0.75	0.47

TABLE I. Comparison of $\overline{C}_D$, $\overline{C}_L$ and St obtained from the coarse, standard and fine grid resolutions for flow around an elliptic cylinder with $AOA = 15^o, 30^o$ and 45^o near a moving wall for $G/D = 0.1$ at $Re = 150$.

Zhu *et al.*[23] for $AOA = 0^o$.

Figure 3 shows the vorticity contours ($\omega = \partial u/\partial y - \partial v/\partial x$) for flow around the elliptic cylinder with $AOA \in [-45^o, 45^o]$ near a moving wall for $G/D = 2.5$ and $Re = 150$. For $AOA = 15^o$(figure 3*a*), a Kármán vortex street is present in the near-wake region, followed by a two-layered wake, while a secondary vortex street occurs far downstream. This wake pattern can be identified as the wake pattern *A*, corresponding to the previous work of Zhu *et al.*[23] for $AOA = 0^o$.

As AOA increases to 30^o (figure 3*b*), the secondary vortex street disappears; the wake structure involves the Kármán vortex street and the two-layered wake. This wake pattern is denoted wake pattern *B*. Figure 4 shows the time-averaged circulation convected into the wake from the top ($\overline{\Gamma}_{top} = \int_s^{s+0.3} u|\omega|dy/T$, where s denotes the cylinder top, 0.3 is chosen to ensure all the vorticity fed into wake being included for integration, and $T = 200$) and the bottom ($\overline{\Gamma}_{bottom} = \int_b^{b-0.3} u|\omega|dy/T$, where b denotes the cylinder bottom) of the cylinder for $AOA = 15^o, 30^o$ and 45^o at $G/D = 2.5$. As AOA increases $\overline{\Gamma}_{bottom}$ decreases gradually while $\overline{\Gamma}_{top}$ remains nearly unchanged as AOA increases from 15^o to 30^o but decreases as AOA increases further to 45^o. Moreover, $\overline{\Gamma}_{bottom}$ is smaller than $\overline{\Gamma}_{top}$, and the difference between them increases with increasing AOA, which is consistent with the strength difference between the vortices shed from the top and the bottom of the cylinder. This can be further visualized by the time-averaged vorticity contours ($\overline{\omega}$) and streamlines as shown in figure 5 for $AOA \in [15^o, 45^o]$. As AOA increases, the clockwise time-averaged recirculation region on the backside of the cylinder becomes larger than the counterclockwise recirculation region, implying that the vortex shed from the top of the cylinder becomes stronger than the one shed from the bottom of the cylinder. Hence the interaction between the clockwise and counterclockwise vortices becomes weaker, stabilizing the wake instability, qualitatively similar to the findings of Paul, Arul Prakash, and Vengadesan[11] for flow around an isolated elliptic cylinder with different AOA. As AOA increases further to 45^o (figure 3*c*), the wake pattern *B* re-

mains but with the onset location of the two-layered wake being located farther downstream than that for smaller AOA (figure 3a and 3b).

The location for the transition from the Kármán vortex street to the two-layered wake for flow over an elliptic cylinder near a moving wall can be identified by the local negative maximum of the time-averaged vertical velocity[23]. Zhu *et al.*[23] found the two-layered wake moving upstream with decreasing G/D. Figure 6 shows time-averaged vertical velocity ($\overline{v}$) contours (a and c) and the corresponding instantaneous vorticity contours (b and d) for $AOA = 15^o$ and $AOA = 30^o$ at $G/D = 2.5$. Here the $\overline{v}$-contours for $AOA = 30^o$ are more asymmetric than for $AOA = 15^o$, coinciding with the observation that the strength difference between the upper and lower vortices increases as AOA increases (see e.g., figure 4). The negative local maximum of $\overline{v}$ (figure 6a for $AOA = 15^o$ and 6c for $AOA = 30^o$) denoted by the dashed-dot lines moves downstream with increasing AOA, showing that the onset location of the two-layered wake is farther away from the cylinder as AOA increases. This can be further illustrated by the spacing ratio H/L, as shown in figures $6(b)$ and $6(d)$, where L denotes the distance between the two successive upper vortices ($V1$ and $V2$) and H represents the distance between the lower vortex ($V3$) and the line connecting $V1$ and $V2$. Durgin and Karlsson[4] and Karasudani and Funakoshi[5] found that H/L increases downstream for flow over an isolated circular cylinder. The transition to the two-layered wake occurs as H/L reaches a critical value at a given downstream location where two successive vortices such as $V1$ and $V2$ impose the convection of vorticity within the vortex $V3$. As a result, this vortex starts to distort and rotate to align with the stream-wise direction, forming the two-layered wake. Zhu *et al.*[23] found that the critical value of H/L is weakly affected by Re and the aspect ratio of the elliptic cylinder but decreases significantly as G/D decreases. In the present work, the critical value of H/L for $AOA = 15^o$ and 30^o is approximately 0.38, slightly smaller than the value 0.41 obtained by Zhu *et al.*[23] for $AOA = 0^o$ at $G/D = 2.5$. It appears that the critical value of H/L is only weakly affected by the rotation of the cylinder, but the location of the critical H/L is farther downstream for $AOA = 30^o$ than for $AOA = 15^o$.

Qualitatively similar behaviors are observed when the cylinder is clockwise rotated (i.e., $AOA = -15^o, -30^o$ and -45^o) as shown in figure $3(d)$-$3(f)$. For $AOA = -15^o$, wake pattern A occurs, i.e., the wake structures contain a Kármán vortex street, a two-layered wake, and a secondary vortex street. As AOA decreases further to -30^o and -45^o, the secondary vortex disappears, implying wake pattern B. Moreover, the onset location of the two-layered wake moves downstream as $|AOA|$ increases, qualitatively similar to that observed for positive AOA (figure 3a-3c).

As G/D decreases to 1.0 (figure 7), no secondary vortex street is present for $AOA \in [-45^o, 45^o]$ due to a stronger wall suppression effect. Here the flow exhibits wake pattern B for all AOAs. The onset location of the two-layered wake moves downstream as $|AOA|$ increases, qualitatively similar to that observed for $G/D = 2.5$ (figure 3). Moreover, for a given AOA, a decrease of G/D leads to the onset location of two-layered wake moving upstream, which is qualitatively similar to that observed by Zhu *et al.*[23] for $AOA = 0^o$.

It should be noted that for the cylinders with $|AOA| = 30^o$ (figure 7b and 7e) and 45^o (figure 7c and 7f), the onset location of the two-layered wake is closer to the cylinder for the negative AOA (clockwise rotated cylinder) than for the positive AOA (counterclockwise rotated cylinder). This is because for positive AOA, the vortices shed from the bottom of the cylinder are not only weakened by the counterclockwise rotation (see, e.g., figure 5) but also by the wall suppression

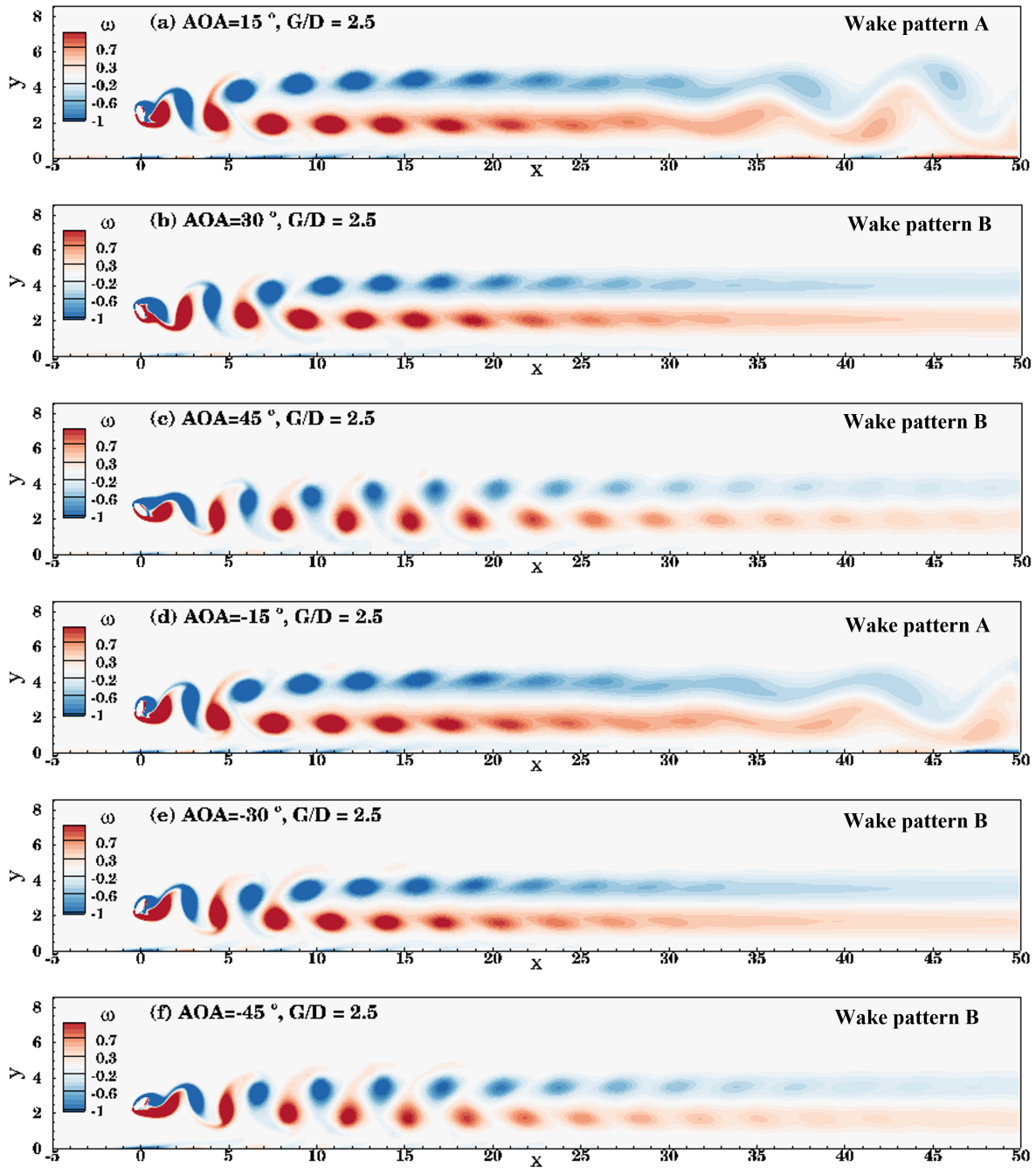

FIG. 3. Instantaneous vorticity contours for flow around an elliptic cylinder with $AOA = (a)15^o$, $(b)30^o$, $(c)45^o$, $(d)-15^o$, $(e)-30^o$ and $(f)-45^o$ near a moving wall for $Re = 150$ at $G/D = 2.5$.

effect. This behavior results in a larger strength difference between the upper and lower vortices for the positive *AOA* than that for the negative *AOA*, where the vortices shed from the bottom of the cylinder is stronger than those shed from the top of the cylinder. Here, for the negative *AOA*, the wall suppression effect weakens the lower vortex, leading to a smaller strength difference between the upper and lower vortices, thus resulting in a stronger interaction. This leads to the distortion

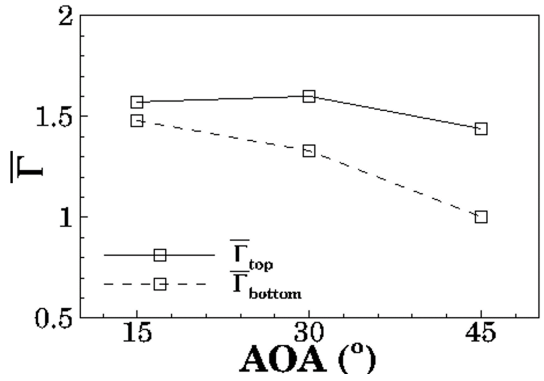

FIG. 4. Time-averaged circulation fed into the wake from the top ($\overline{\Gamma}_{top}$) and the bottom ($\overline{\Gamma}_{bottom}$) of the cylinder for $AOA = 15^o, 30^o$ and 45^o for $Re = 150$ at $G/D = 2.5$.

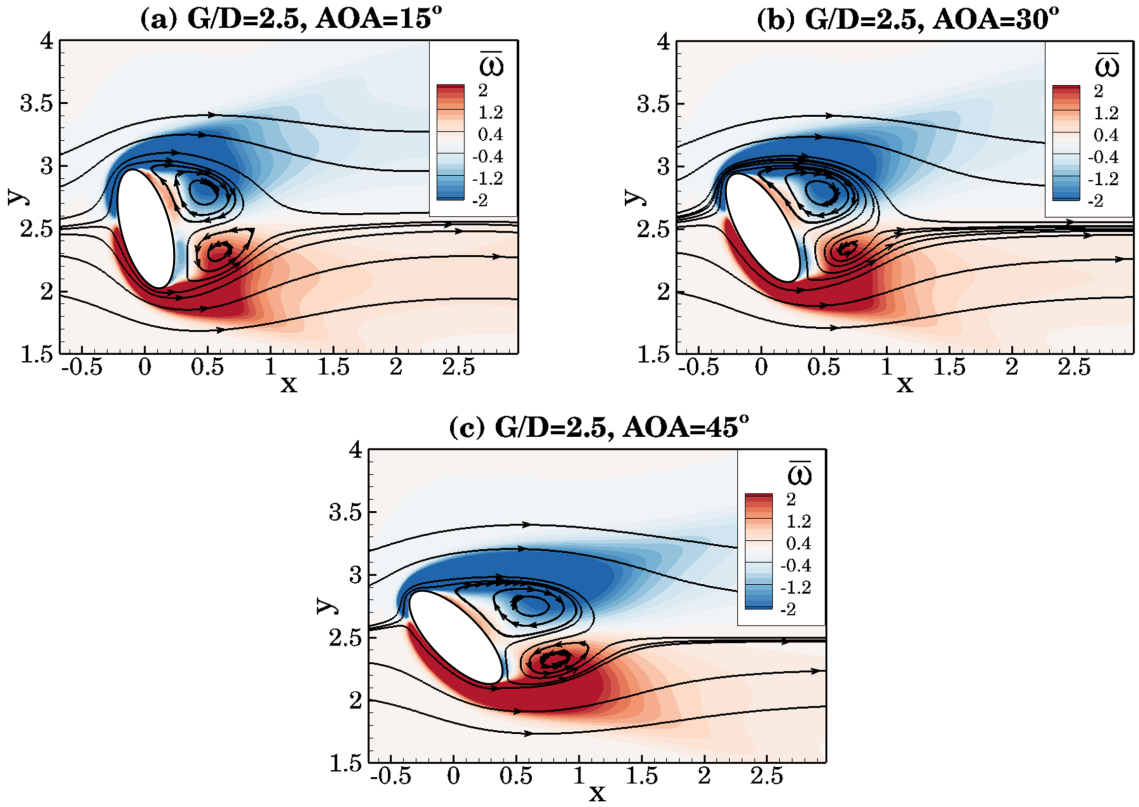

FIG. 5. Time-averaged vorticity contours and streamlines for flow around an elliptic cylinder with $AOA = (a)15^o, (b)30^o$ and $(c)45^o$ near a moving wall for $Re = 150$ at $G/D = 2.5$.

and rotation of the vortices aligned with the stream-wise direction being closer to the cylinder.

As G/D decreases further to 0.6, for $AOA \in [-15^o, 45^o]$ (figure 8a-8d), the vortex shed from the bottom part of the cylinder follows immediately the vortex shed from the top of the cylinder, forming a vortex pair moving downstream and deflecting away from the wall. This wake pattern can be classified as wake pattern C^{23}. Furthermore, an increase of $|AOA|$ weakens the wall sup-

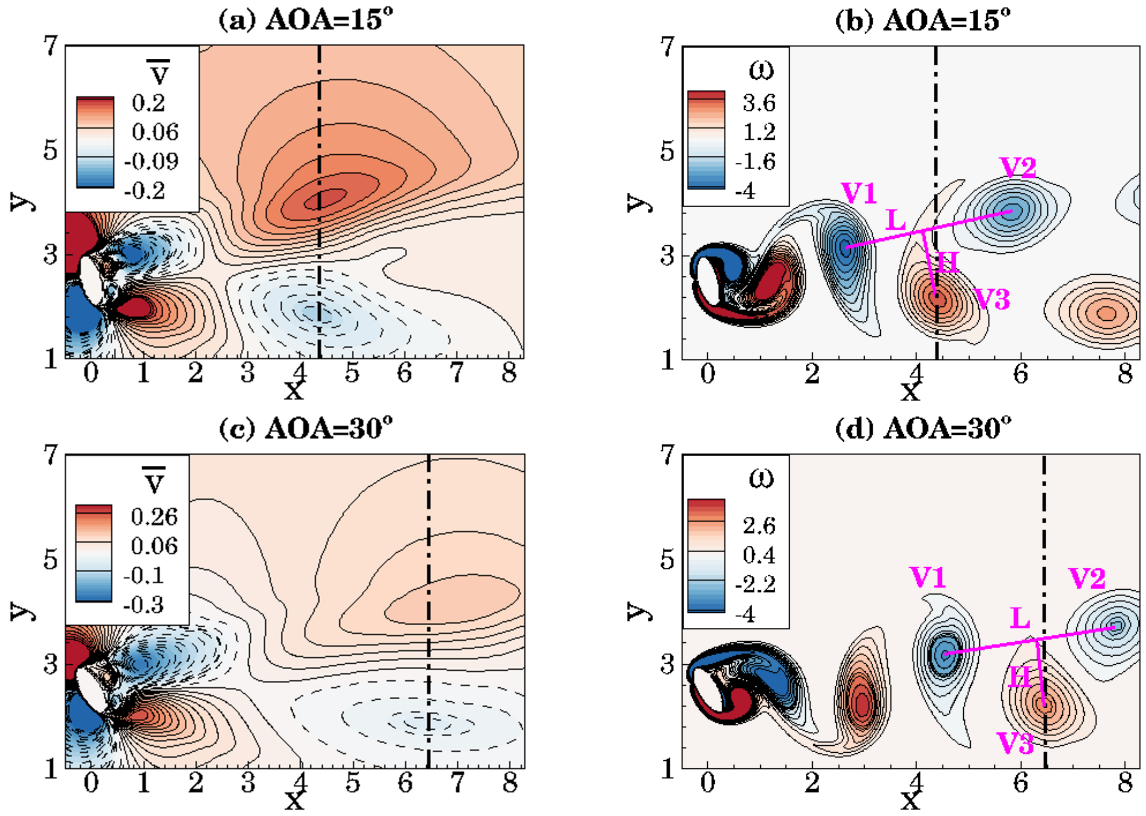

FIG. 6. Time-averaged vertical velocity $\bar{v}$ contours for flow around an elliptic cylinder with (a) $AOA = 15^o$ and (c) $AOA = 30^o$ near a moving wall at $G/D = 2.5$ as well as the corresponding instantaneous vorticity contours (b) and (d); the dashed-dot line denotes the transition location from the Kármán vortex street to the two-layered wake.

pression effect on the near-wall vortex shedding, thus resulting in a smaller distance between each vortex pair. Table II shows the time-averaged angular positions of the front stagnation point (θ_F), the upper (θ_U) and lower (θ_L) separation points for $G/D = 0.6$ and $AOA \in [15^o, 45^o]$ at $Re = 150$. Here the angular position is measured from the semi-minor axis of the cylinder where $\theta = 0^o$. As AOA increases from 15^o to 45^o, the values of θ_U, θ_L and θ_F decrease, implying that the up and lower separation points move downwards along the backside of the cylinder while the front stagnation point moves upwards along the front of the cylinder, causing a smaller offset of the vortex pairs away from the moving wall (figure 8a-8c).

For $AOA = -30^o$ and -45^o (figure 8e-8f), the flow becomes steady and the vortex shedding is absent. It appears that in addition to the wall suppressing the near-wall vortex shedding, there is a larger blockage effect between the moving wall and the backside of the cylinder for $AOA = -45^o$ and -30^o than for $AOA = -15^o$. As a result, the vortex shedding is completely suppressed for $AOA = -30^o$ and -45^o.

Figure 9 shows the distribution of the steady wake pattern where vortex shedding is absent, as well as wake patterns A, B and C within the (G/D, AOA)-space for $Re = 150$. Here the results for $AOA = 0^o$ were obtained from the previous work of Zhu *et al.*[23]. For $AOA \in [-15^o, 15^o]$, the flow exhibits a transition sequence of 'wake pattern A' $\rightarrow$ 'wake pattern B' $\rightarrow$ 'wake pattern C' $\rightarrow$

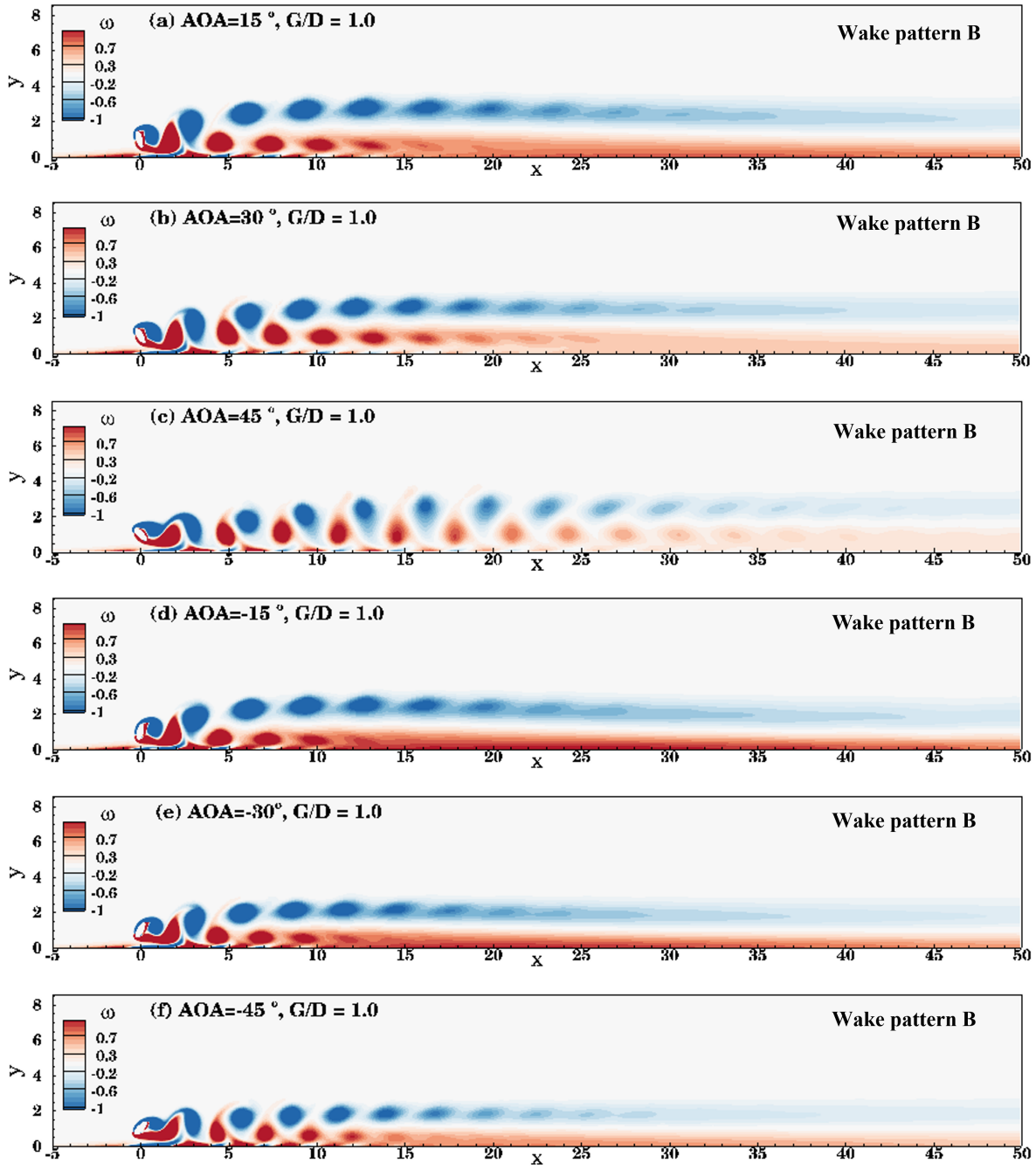

FIG. 7. Instantaneous vorticity contours for flow around an elliptic cylinder with $AOA = (a)15^o$, $(b)30^o$, $(c)45^o$, $(d)-15^o$, $(e)-30^o$ and $(f)-45^o$ near a moving wall for $Re = 150$ at $G/D = 1.0$.

'steady wake' as G/D decreases.

For $AOA = \pm 30^o$, wake pattern B is found for $G/D \in [0.8, 2.5]$. As G/D decreases from 0.8 to 0.7, there is a transition from wake pattern B to wake pattern C for $AOA = \pm 30^o$. It should be noted that for $AOA = -30^o$, there is a further transition from wake pattern C to the steady wake flow regime as G/D decreases from 0.7 to 0.6. For $AOA = 45^o$, there is a transition from wake pattern B to wake pattern C as G/D decreases from 0.8 to 0.7 while for $AOA = -45^o$, this transition

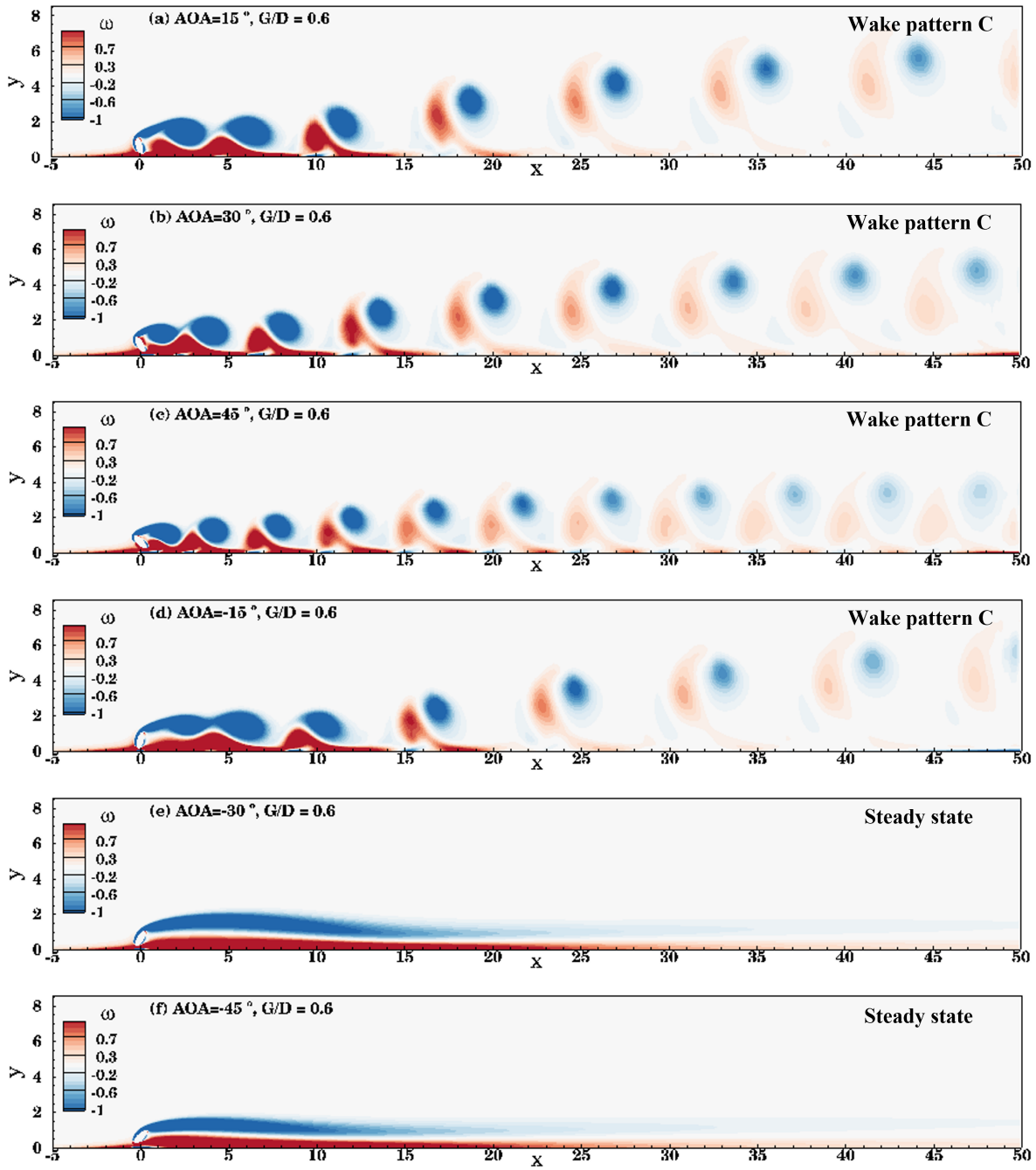

FIG. 8. Instantaneous vorticity contours for flow around an elliptic cylinder with $AOA = (a)15^o$, $(b)30^o$, $(c)45^o$, $(d)-15^o$, $(e)-30^o$ and $(f)-45^o$ near a moving wall for $Re = 150$ at $G/D = 0.6$.

takes place as G/D decreases from 1.0 to 0.9. Moreover, a further transition from wake pattern C to the steady wake flow regime takes place as G/D decreases from 0.7 to 0.6 for $AOA = -45^o$.

Overall, the clockwise and counter clockwise rotation of the cylinder weaken the vortices shed from the top and bottom of the cylinder, respectively. For $G/D \geq 1.0$, both the clockwise and the counterclockwise rotation of the cylinder leads to similar wake transitions. For $G/D < 1.0$, the clockwise rotation of the cylinder leads to more transitions than those for the counterclockwise

G/D	AOA	θ_U	θ_L	θ_F
0.6	15^o	83.5^o	-80.6^o	-123.5^o
0.6	30^o	80.4^o	-84.2^o	-135.5^o
0.6	45^o	73.6^o	-87.1^o	-180.2^o

TABLE II. Time-averaged angular positions of the front stagnation point (θ_F), the upper (θ_U) and lower (θ_L) separation points for $G/D = 0.6$ and $AOA = 15^o, 30^o$ and 45^o at $Re = 150$. Here the angular position is measured from the semi-minor axis of the cylinder where $\theta = 0^o$.

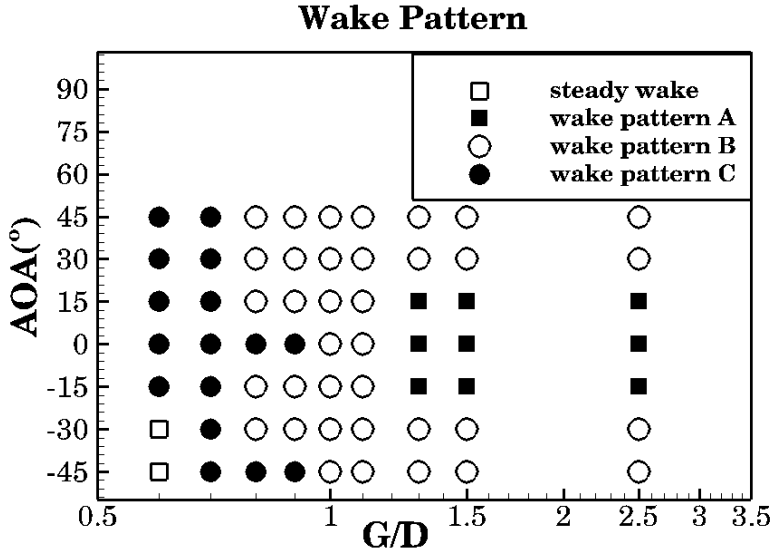

FIG. 9. Distribution of the wake patterns, i.e., steady wake (□), wake pattern A (■), wake pattern B (○), wake pattern C (●) within the (G/D, AOA)-space.

rotation of the cylinder due to a stronger suppression effect on the near-wall vortex shedding for the clockwise rotation.

The combined effect of AOA and G/D on the critical Reynolds number Re_c for the onset of vortex shedding has been investigated for $AOA = 0^o$ and $\pm 45^o$ for $G/D = 0.6$ and 0.9. For $G/D = 0.9$, Re_c equals to 77.5 ± 2.5, 72.5 ± 2.5 and 82.5 ± 2.5 for $AOA = 0^o, 45^o$ and -45^o, respectively. This implies that a counterclockwise rotation of the cylinder results in a smaller Re_c for $AOA = 45^o$ than for $AOA = 0^o$ due to an increase of the gap between the cylinder bottom and the moving wall, which results in a weaker wall suppression effect on the vortex shedding for $AOA = 45^o$ than for $AOA = 0^o$. A clockwise rotation of the cylinder leads to a larger Re_c for $AOA = -45^o$ than for $AOA = 0^o$ due to a decrease of the gap between the cylinder back and the moving wall which results in a stronger wall suppression effect on the vortex shedding for $AOA = -45^o$ than for $AOA = 0^o$. As G/D decreases to 0.6, Re_c increases to 117.5 ± 2.5 for $AOA = 0^o$ and 45^o and more than 150 for $AOA = -45^o$. This shows that the onset of vortex shedding is only weakly affected by a counterclockwise rotation of the cylinder due to the strong wall suppression effect, while a clockwise rotation of the cylinder leads to a much larger Re_c than for $AOA = 0^o$.

B. Instantaneous drag and lift forces acting on the cylinder

1. Counterclockwise rotation of the cylinder

Figure 10 shows the time history of C_D (left column) and C_L (right column) for flow over an elliptic cylinder with $AOA = 15^o, 30^o$ and 45^o near a moving wall for $G/D = 0.6, 1.0$ and 2.5, at $Re = 150$ (i.e., for the counterclockwise rotated cylinder). For $G/D = 2.5$, every second crest value of C_D (figure 10a) is larger than the other. The smaller crest values are caused by the vortices shed from the bottom part of the cylinder, while the larger crest values are caused by the vortices shed from the top of the cylinder; this coincides with the time-averaged vorticity and streamlines shown in figure 5. Moreover, the frequency of C_L is half of C_D, coinciding with the Kármán vortex shedding in the near-wake region as shown in figure $3(a)$-$3(c)$. The difference between the crest and trough values (hereafter refered to as fluctuation height) of C_D and C_L decreases as *AOA* increases, coinciding with the weakening of the vortex shedding (figure 3a-3c). Furthermore, the crest values of C_L first increase as *AOA* increases from 15^o to 30^o and then decrease as *AOA* increases further to 45^o. This behavior can be explained by two major mechanisms: i) an increase of *AOA* leads to an increase of the vertical component (C_L) of the total force acting on the cylinder, resulting in an increase of the crest values of C_L as *AOA* increases from 15^o to 30^o; ii) an increase of *AOA* weakens the vortex shedding, resulting in a decrease of the magnitude of the total force, thus leading to a decrease of the crest values of C_L as *AOA* increases from 30^o to 45^o.

As G/D decreases to 1.0, as shown in figure $10(c)$, the smaller crest values (marked by a and c for $AOA = 15^o$ and 30^o, respectively) of C_D are caused by the vorticies shed from the top of the cylinder while the larger crest values of C_D (marked by b and d for $AOA = 15^o$ and 30^o, respectively) are caused by the vortices shed from the bottom part of the cylinder. This is opposite to that observed for $G/D = 2.5$. Figure $11(a)$-$11(c)$ show the corresponding time-history of the circulation fed into the wake from the top (Γ_{top}) and the bottom (Γ_{bottom}) of the cylinder with corresponding markers a, b, c, d, e and f in figure $10(c)$. Here Γ_{bottom} decreases significantly as *AOA* increases while Γ_{top} is weakly affected as *AOA* increases from 15^o to 30^o but decreases significantly as *AOA* increases further to 45^o. Moreover, the peak values of Γ_{top} become larger than Γ_{bottom} when *AOA* increases, and the difference between their peak values increases with increasing *AOA*. This behavior is consistent with the time-averaged circulation observed for $G/D = 2.5$ (figure 4), showing that a counterclockwise rotation of the cylinder leads to the upper vortices being stronger than the lower vorticies. Figure $12(a)$, $12(b)$, $12(c)$, and $12(d)$ show the instantaneous vorticity contours and streamlines corresponding to the crest values marked as a, b, c, and d in figure $10(c)$. It is clearly shown that the vortex core (region with maximum vorticity) is closer to the cylinder for the vortex shed from the cylinder bottom than for the vortex shed from the cylinder top. This leads to a larger crest value of C_D when the wake is dominated by the lower vortex (figure 12b and 12d) than when the wake is dominated by the upper vortex (figure 12a and 12c) for $AOA = 15^o$ and 30^o despite the fact that the upper vortex is stronger than the lower vortex.

For $AOA = 45^o$ (figure 10c), the smaller crest values (marked by e) are caused by the vorticies shed from the bottom part of the cylinder while the larger crest values (marked by f) are caused by the vortices shed from the top of the cylinder. The corresponding instantaneous vorticity contours and streamlines are shown in figures $12(e)$ and $12(f)$. Here an increase of *AOA* leads to a decrease

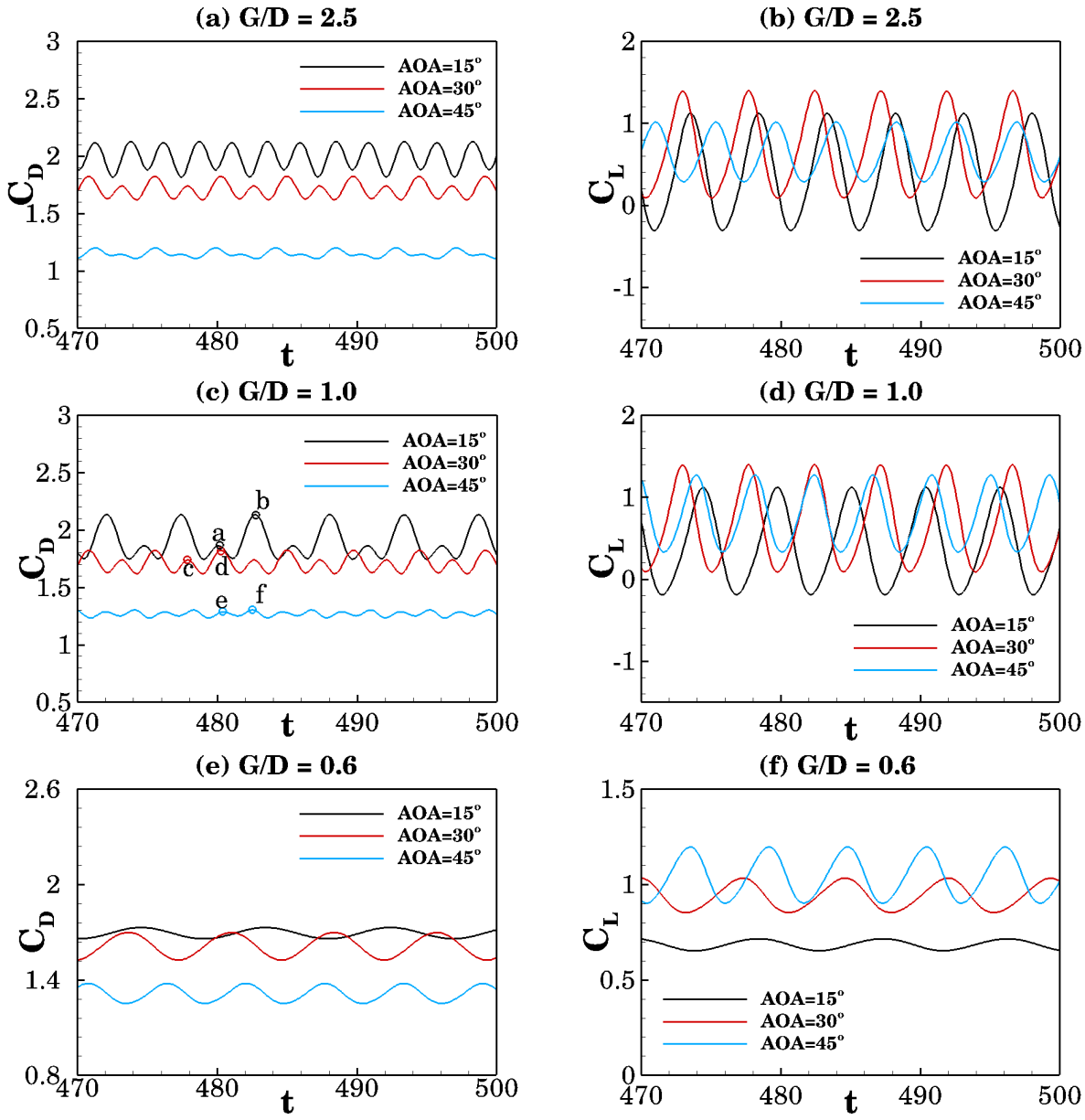

FIG. 10. Time history of C_D (left column) and C_L (right column) for flow around an elliptic cylinder with $AOA = 15^o, 30^o$ and 45^o near a moving wall for $G/D =$ (a-b) 2.5, (c-d) 1.0, and (e-f) 0.6 at $Re = 150$.

of the gap flow velocity, i.e., a smaller circulation fed into the lower vortex as shown in figure $11(c)$, resulting in a smaller recirculation region of the lower vortex on the backside of the cylinder (figure 12*e*), which leads to smaller crest values of C_D for $AOA = 45^o$ than for $AOA = 15^o$ and 30^o.

The corresponding lift coefficient C_L is shown in figure $10(d)$. Here the fluctuation heights of C_L decrease as AOA increases while the crest values of C_L first increase and then decrease as AOA increases from 15^o to 45^o, qualitatively similar to the observation for $G/D = 2.5$ (figure 10*b*). It should be noted that for $G/D = 1.0$, the crest values of C_L are larger for $AOA = 45^o$ than for $AOA = 15^o$ while an opposite behavior is observed for $G/D = 2.5$ (figure 10*b*). It appears that a decrease of G/D from 2.5 to 1.0 leads to a stronger blockage effect in the gap[18], resulting in larger

crest values of the pressure acting on the cylinder front, thus forming larger crest values of C_L for $AOA = 45^o$ at $G/D = 1.0$.

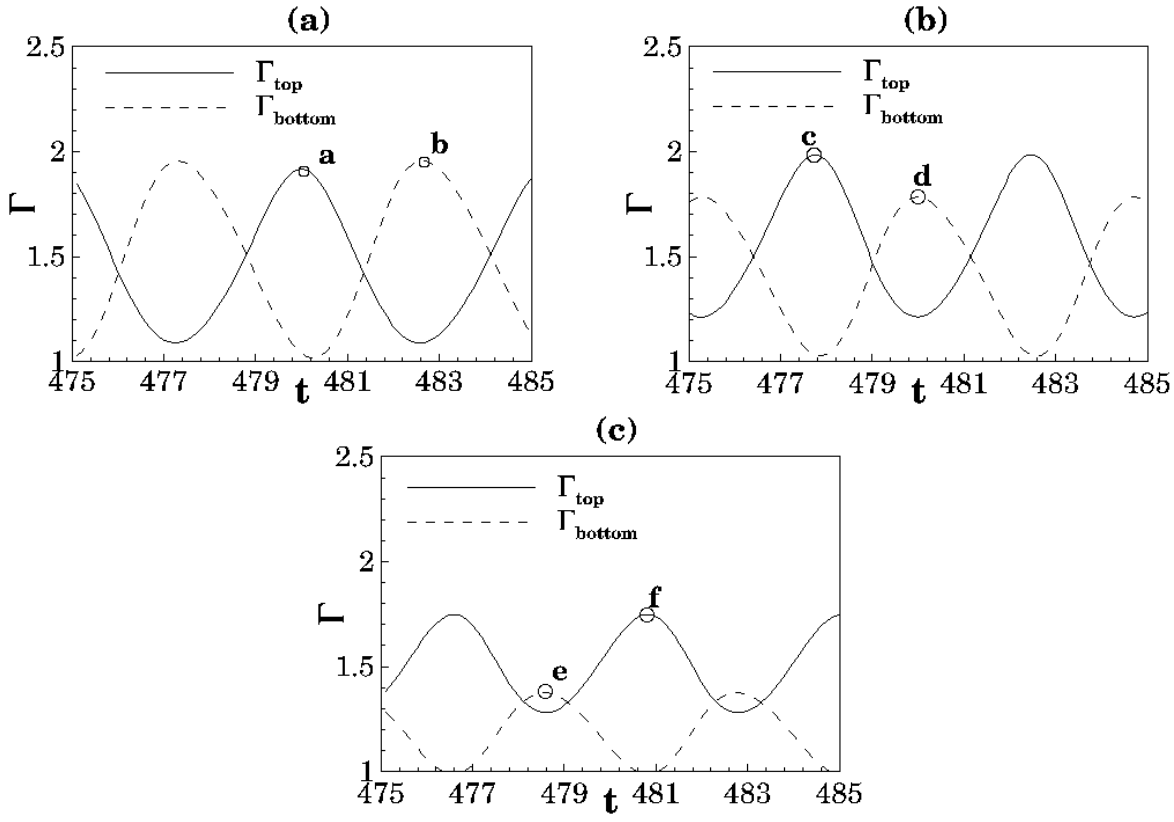

FIG. 11. Time history of circulation fed into the wake from the top (Γ_{top}) and the bottom (Γ_{bottom}) of the cylinder with $AOA =$ (a) 15^o, (b) 30^o and (c) 45^o with markers corresponding to those in figure $10(c)$ for $G/D = 1.0$ and $Re = 150$.

As G/D decreases further to 0.6 (figure $10e$-$10f$), the values of C_D and C_L fluctuate with the same frequency for a given AOA. This is consistent with the observed pair-wise vortex shedding (wake pattern C) shown in figures $8(a)$-$8(c)$. The fluctuation heights of C_D (figure $10e$) increase as AOA increases from 15^o to 30^o due to stronger vortex shedding (figure $8a$-$8b$), which leads to a larger pressure difference between the front and the backside of the cylinder. As AOA increases further to 45^o, this fluctuation height decreases slightly due to the decrease of the horizontal component (C_D) of the total force acting on the cylinder, which counteracts the increase of the magnitude of the total force caused by a stronger vortex shedding (figure $8c$). Moreover, both the fluctuation heights and the crest values of C_L (figure $10f$) decrease as AOA increases due to stronger vortex shedding and the increase of the vertical component of the total force.

2. Clockwise rotation of the cylinder

Figure 13 shows the time history of C_D (left column) and C_L (right column) for $AOA = -15^o, -30^o$ and -45^o at $G/D = 0.6, 1.0$ and 2.5 (i.e., for the clockwise rotated cylinder). For

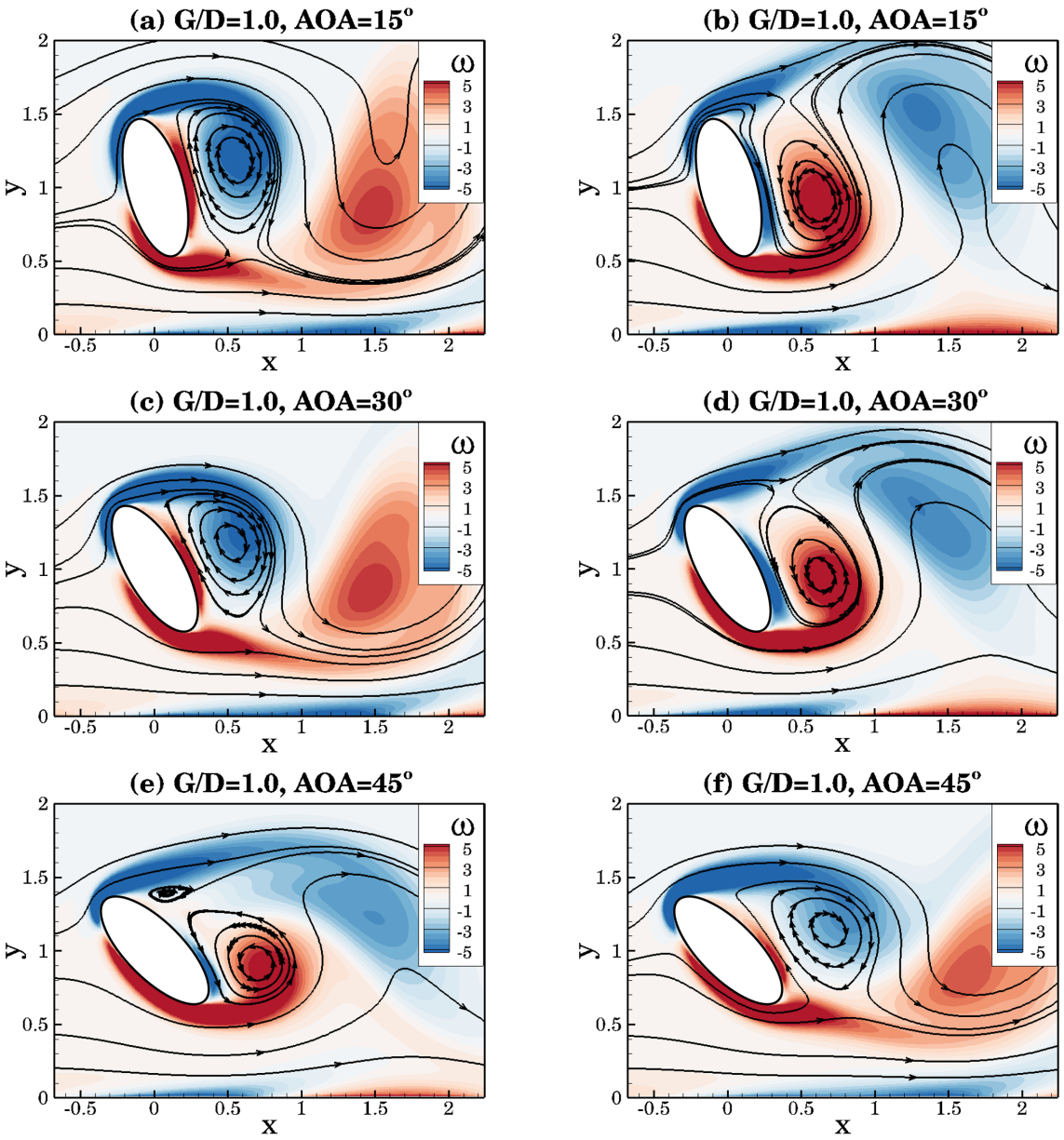

FIG. 12. Instantaneous vorticity contours and streamlines for flow around an elliptic cylinder with $AOA =$ (a-b) 15^o, (c-d) 30^o and (e-f) 45^o near a moving wall at different instants (a-f) (marked in figure 10c) for $G/D = 1.0$ and $Re = 150$.

$G/D = 2.5$, every second crest value of C_D (figure 13a) is larger than the other. The larger crest values of C_D (marked by a in figure 13a) are caused by the vortices shed from the bottom part of the cylinder while the smaller crest values (marked by b in figure 13a) are caused by the vortices shed from the top of the cylinder. Figures 14(a) and 14(b) show the instantaneous vorticity contours and streamlines corresponding to the marked crest values a and b in figure 13(a). The magnitude of the vorticity and the recirculation region on the backside of the cylinder are larger for the vortex shed from the bottom of the cylinder than for the vortex shed from the top of the cylinder. This leads to a larger crest value of C_D caused by the lower vortex than the crest value

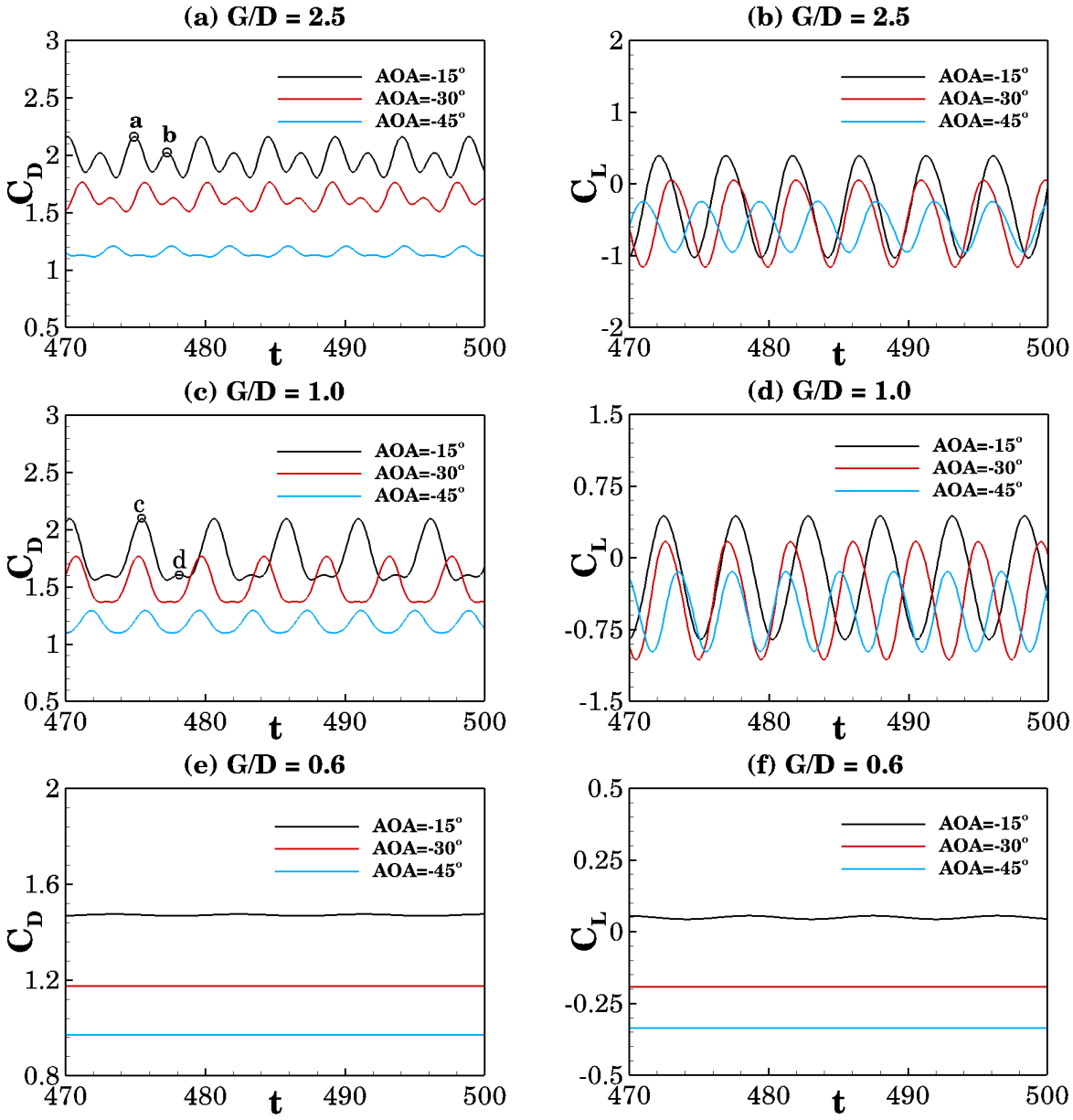

FIG. 13. Time history of C_D (left column) and C_L (right column) for flow around an elliptic cylinder with $AOA = \pm 15^o, \pm 30^o$ and $\pm 45^o$ near a moving wall for $G/D =$ (a-b) 2.5, (c-d) 1.0, and (e-f) 0.6 at $Re = 150$.

of C_D caused by the upper vortex. Moreover, both the fluctuation heights and the crest values of C_L (figure 13b) decreases as AOA increases due to the weakening of the vortex shedding. The frequency of C_L is half of C_D, coinciding with the Kármán vortex shedding in the near-wake region (figure 3d-3f).

As G/D decreases to 1.0, the crest values of C_D (figure 13c) caused by the vortices shed from the bottom part of the cylinder (e.g., marked by c for $AOA = -15^o$) are larger than those caused by the vortices shed from the top of the cylinder (e.g., marked by d for $AOA = -15^o$), as visualized by the corresponding vorticity contours and streamlines in figure 14(c) and 14(d). This behavior is qualitatively similar to that observed for $G/D = 2.5$. It is worth noting that the crest values

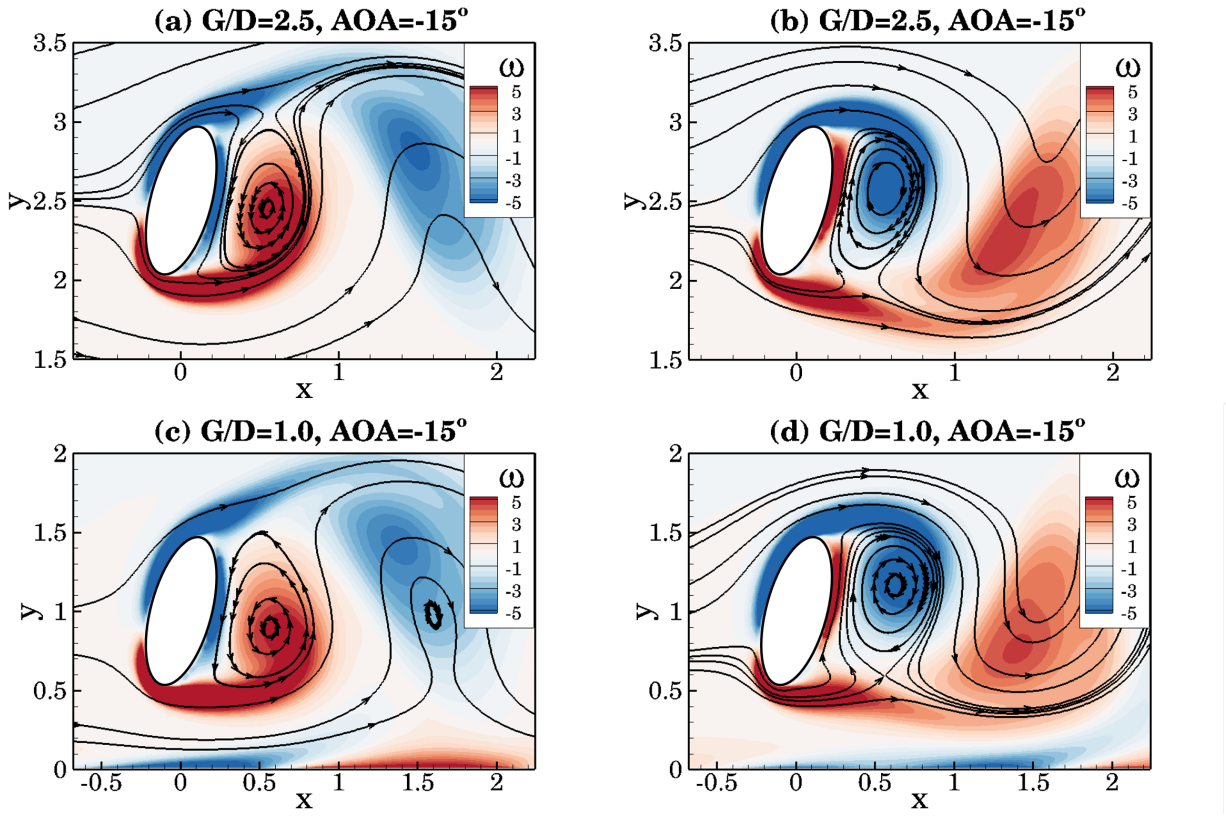

FIG. 14. Instantaneous vorticity contours and streamlines for flow around an elliptic cylinder with $AOA = -15^o$ near a moving wall for $G/D =$ (a-b) 2.5 and (c-d) 1.0 at $Re = 150$.

of C_D caused by the upper vortices become small for $G/D = 1.0$, relative to those at $G/D = 2.5$ (figure 13a). This can be further explained by the time-averaged vorticity contours and streamline shown in figure 15 for $AOA = -15^o$ at $G/D = 2.5$ and 1.0. A decrease of G/D from 2.5 to 1.0 leads to a weaker upper vortex with a smaller recirculation region on the backside of the cylinder, thus resulting in the small crest values for $G/D = 1.0$ (marked by d in figure 13c). Moreover, both the fluctuation heights and the crest values of C_L (figure 13d) decrease as AOA increases, which is a qualitatively similar behavior as that observed for $G/D = 2.5$.

As G/D decreases further to 0.6 (figure 13e-13f), the values of C_D and C_L are nearly time-independent, coinciding with the long shear layer in the near-wake region for $AOA = -15^o$ and the absence of vortex shedding behind the cylinder for $AOA = -30^o$ and -45^o shown in figure $8(d)$-$8(f)$.

Overall, the drag coefficient C_D exhibits a qualitatively similar behavior for positive (figure 10a and 10c) and negative (figure 13a and 13c) AOA at $G/D = 2.5$ and 1.0. This behavior can be summarized as follows; i) every second crest value is larger than the other; ii) both the fluctuation heights and the crest values of C_D decrease with increasing $|AOA|$; iii) the frequency of C_D is double of C_L. At $G/D = 0.6$, the C_D fluctuates with the same frequency as C_L for positive AOA (figure 10e) but remains nearly constant for negative AOA (figure 13e) due to strong suppression effect between the moving wall and the backside of the cylinder. As for the lift coefficient (C_L), the fluctuation height exhibits a similar behavior, i.e., it decreases as AOA increases for positive

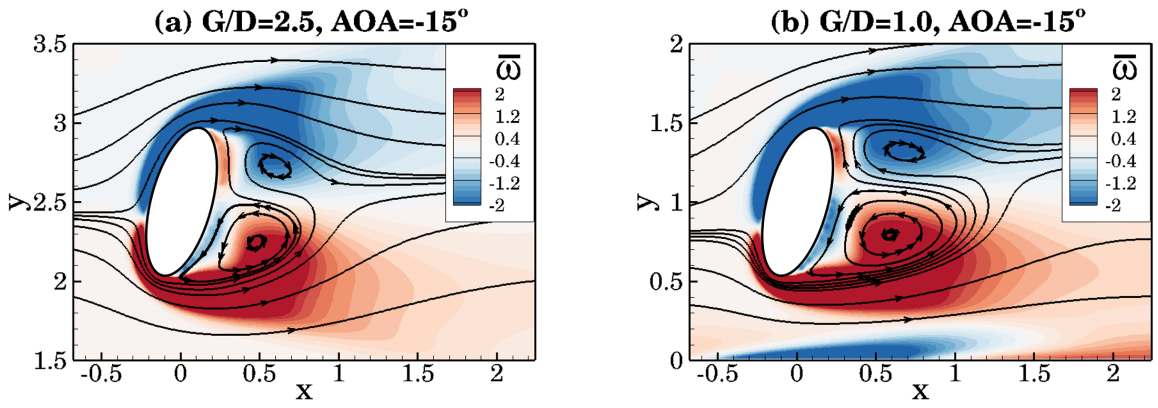

FIG. 15. Time-averaged vorticity contours and streamlines for flow around an elliptic cylinder with $AOA = -15^o$ near a moving wall for $G/D =$ (a) 2.5 and (b) 1.0 at $Re = 150$.

and negative AOA at $G/D = 2.5$, 1.0 and 0.6. However, for $G/D = 2.5$ and 1.0, as $|AOA|$ increases, the crest values of C_L first increase and then decrease for positive AOA while the corresponding crest values decrease for negative AOA.

C. Time-averaged drag force acting on the cylinder

1. Counterclockwise rotation of the cylinder

Figure 16(a) shows the time-averaged drag coefficient ($\overline{C}_D$) for $G/D \in [0.6, 2.5]$ and $AOA = 0^o, 15^o, 30^o$ and 45^o at Re = 150. The results obtained from $AOA = 0^o$ by Zhu *et al.*[23] are included for comparison. For $AOA = 15^o$, the value of $\overline{C}_D$ increases gradually for $G/D \in [0.6, 1.5]$, except for a drag reduction observed for $G/D \in [0.74, 0.8]$. This is qualitatively similar to that observed by Zhu *et al.*[23] for $AOA = 0^o$, who explained the intermediate drag reduction with the strength of the vortex shedding behind the cylinder; as G/D decreases from 0.8 to 0.74, the shear layer on the bottom wall leads to a stronger interaction between the vortices shed from the top and bottom part of the cylinder, causing a higher vortex shedding frequency, thus forming stronger vortices shed from the bottom part of the cylinder, which results in an increase of $\overline{C}_D$. It should be noted that for $G/D \leq 1.0$, $\overline{C}_D$ is smaller for $AOA = 0^o$ than for $AOA = 15^o$ while for $G/D > 1.0$, $\overline{C}_D$ is larger for $AOA = 0^o$ than for $AOA = 15^o$. The mechanism underpinning this behavior will be further discussed in section $C2$. In the work of Zhu *et al.*[23], the physical mechanisms for the variation of $\overline{C}_D$ with G/D are mainly explained by the vortex shedding behind the cylinder, i.e., stronger vortices resulting in a larger $\overline{C}_D$. In the present work, the variation of the time-averaged pressure drag force acting on the front and the backside of the cylinder is further investigated for different G/D and AOA to clarify the combined effect of the flow over the front of the cylinder and the vortex shedding behind the cylinder on $\overline{C}_D$.

Figure 16(b) shows the horizontal component ($P_{x,f}$) of the time-averaged pressure force resulting from integrating the pressure over the front of the cylinder for $AOA = 0^o, 15^o, 30^o$ and 45^o with $G/D \in [0.6, 2.5]$ at Re = 150. For $AOA = 15^o$, the value of $P_{x,f}$ decreases as G/D increases due to

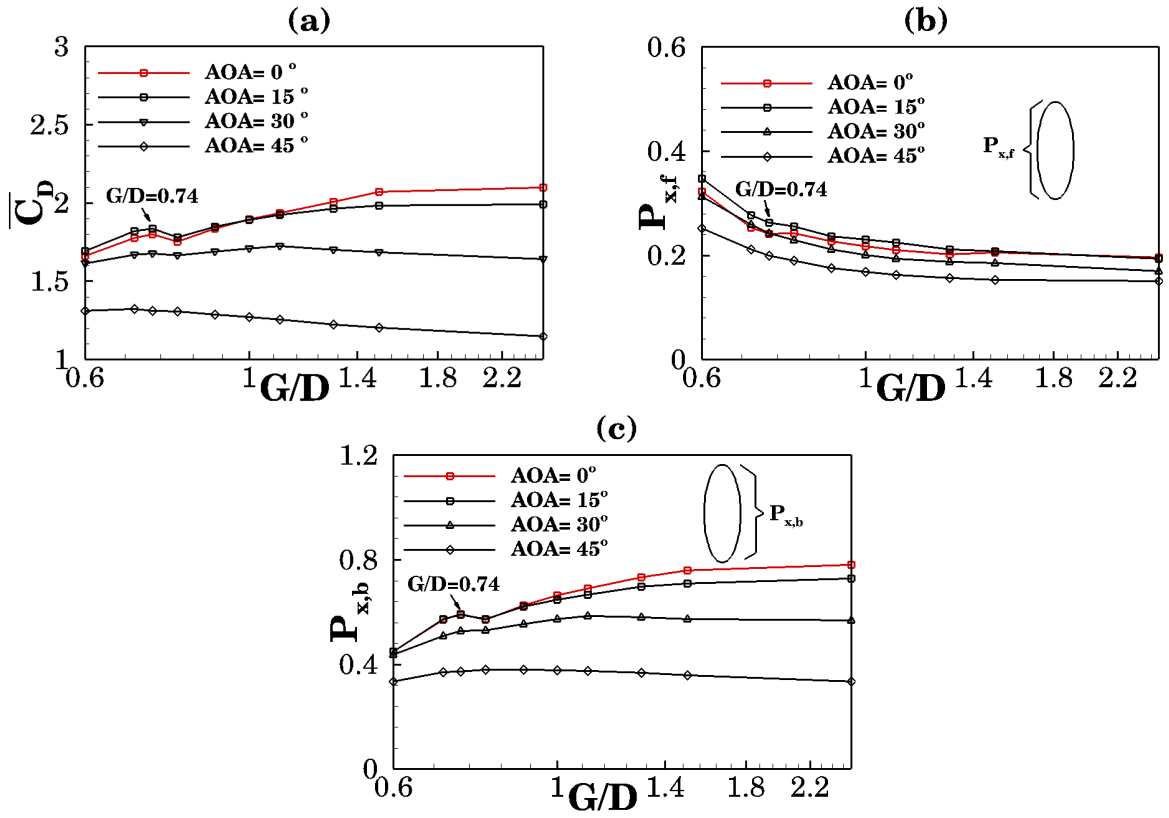

FIG. 16. Variation of $(a)\ \overline{C}_D$, $(b)\ P_{x,f}$ and $(c)\ P_{x,b}$ for flow around an elliptic cylinder with $AOA = \pm 15^o, \pm 30^o$ and $\pm 45^o$ near a moving wall for $G/D \in [0.6, 2.5]$ at $Re = 150$.

a decrease of gap flow velocity[16], which results in a smaller pressure force acting on the near-wall part of the cylinder front. This can be further visualized by the distribution of the time-averaged pressure coefficient $\overline{C}_p$ around the elliptic cylinder shown in figure $17(a)$ for $AOA = 15^o$ with $G/D \in [0.6, 0.8]$; here C_p is defined by $(p - p_0)/(0.5\rho U^2)$ where p_0 is the pressure at the outlet of the computational domain. The time-averaged pressure coefficient $\overline{C}_p$ are plotted such that the value of line at a given point is proportional to the normal distance from the cylinder surface. The value of $\overline{C}_p$ on the near-wall part of the cylinder front decreases as G/D increases. This coincides with the decrease of $P_{x,f}$ with increasing G/D.

Figure $16(c)$ shows the horizontal component ($P_{x,b}$) of the time-averaged pressure force obtained by integrating the pressure over the backside of the cylinder for $AOA = 0^o, 15^o, 30^o$ and 45^o with $G/D \in [0.6, 2.5]$ at Re = 150. It should be noted that the pressure behind the cylinder is overall negative (the reference pressure p_0 at the outlet of the computational domain is zero). Hence the resulting horizontal component $P_{x,b}$ acts in the positive x-direction, i.e., in the same direction as $P_{x,f}$. For $AOA = 15^o$, the value of $P_{x,b}$ increases as G/D increases due to the weakening of the wall suppression effect, except for a sudden drop for $G/D \in [0.74, 0.8]$. This behavior coincides with that observed for $\overline{C}_D$ for $AOA = 15^o$ (figure 16a). Since the increase of $P_{x,b}$ is larger than the decrease of $P_{x,f}$ as G/D increases, the variation of $\overline{C}_D$ with G/D is mainly affected by the strength of the vortices shed from the cylinder. The physical mechanism underpinning the sudden drop of $P_{x,b}$ was previously explained by Zhu *et al.*[23] for $AOA = 0^o$ at $Re = 150$; at small G/D (e.g., for

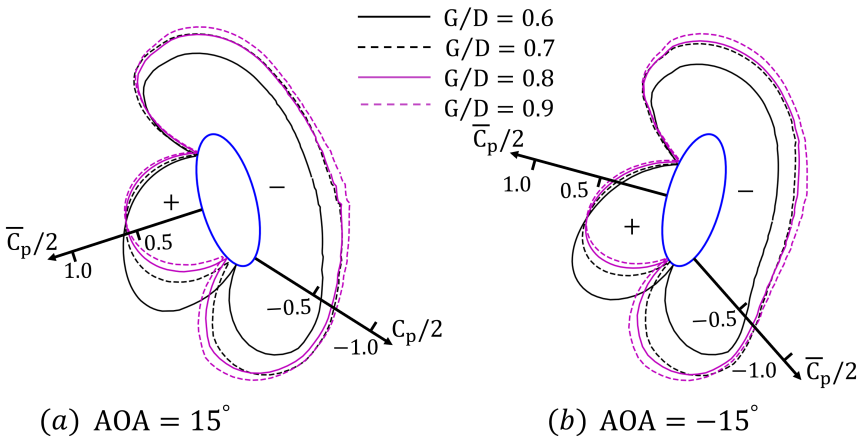

FIG. 17. Time-averaged pressure coefficient $\overline{C}_p$ around the elliptic cylinder with (a) $AOA = 15^o$ and (b) $AOA = -15^o$ at $G/D = 0.6, 0.7, 0.8$ and 0.9 for Re = 150. Here the value of $\overline{C}_p$ at a given point of the line is proportional to the normal distance from the cylinder surface. The value of $\overline{C}_p$ is calculated with a reference pressure of zero at the outlet.

$G/D \in [0.6, 0.74]$), the bottom-wall shear layers cause the vortex shed from the bottom part of the cylinder to roll up such that it is located closer to the vortex shed from the top of the cylinder. This results in an increase of the vortex shedding frequency (i.e., Strouhal number $St = fD/U$; where f denotes the vortex shedding frequency), which counteracts the decrease of St induced by the enhanced wall suppression effect (as G/D decreases from 0.8 to 0.74), thus resulting in a nearly constant St for $G/D \in [0.74, 0.8]$. This behavior is also present for $AOA = 15^o$ as shown in figure $19(c)$, showing the variation of St with G/D for $AOA \in [-45^o, 45^o]$ at $Re = 150$; St remains nearly constant for $G/D \in [0.74, 0.8]$ for $AOA = 15^o$.

For $AOA = 30^o$, $\overline{C}_D$ (figure $16a$) increases slightly as G/D increases from 0.6 to 1.1, except for a small drag reduction observed for $G/D \in [0.74, 0.8]$ as observed for $AOA = 0^o$ and $AOA = 15^o$. The variation of $P_{x,f}$ (figure $16b$) and $P_{x,b}$ (figure $16c$) with G/D is almost the same as for $AOA = 15^o$, and, by the same argument as for these $AOAs$, the increase of $\overline{C}_D$ with increasing G/D is mainly caused by the increase of $P_{x,b}$ due to weakening of the wall suppression effect. However, the sudden drop of $P_{x,b}$ observed for $AOA = 15^o$ for $G/D \in [0.74, 0.8]$ is nearly absent here; it appears that a counterclockwise rotation of the cylinder of $AOA = 30^o$ weakens the interaction between the bottom-wall shear layers and the vortices shed from the bottom part of the cylinder. This is confirmed by the decrease of St (as G/D decreases from 0.8 to 0.74) shown in figure $19(b)$. Thus, by comparing $P_{x,f}$, $P_{x,b}$ and $\overline{C}_D$ in figure $16(b)$, $16(c)$ and $16(a)$, respectively, the drag reduction for $G/D \in [0.74, 0.8]$ for $AOA = 30^o$ is mainly due to the decrease of the $P_{x,f}$.

As G/D increases from 1.1 to 2.5 for $AOA = 30^o$, $\overline{C}_D$ decreases slightly, coinciding with the decrease of both $P_{x,f}$ and $P_{x,b}$. It appears that an increase of G/D for $G/D > 1.1$ leads to a decrease of the gap flow velocity, which results in a smaller pressure on the front of the cylinder and a weaker vortex shedding behind the bottom part of the cylinder, thus causing the decrease of $P_{x,f}$ and $P_{x,b}$, respectively. This slight decrease of $\overline{C}_D$ with increasing G/D is absent for $AOA = 0^o$

and 15^o.

For $AOA = 45^o$, the values of $\overline{C}_D$ remain nearly constant for $G/D \in [0.6, 0.7]$ due to the balance between the decrease of $P_{x,f}$ and the increase of $P_{x,b}$, as shown in figure 16(b) and 16(c), respectively. As G/D increases further, $\overline{C}_D$ decreases, coinciding with the decrease of both $P_{x,f}$ and $P_{x,b}$, which is qualitatively similar to the observation for $AOA = 30^o$ for $G/D \in [1.1, 2.5]$. Moreover, the decrease of $\overline{C}_D$ with increasing G/D occurs at a smaller G/D for $AOA = 45^o$ than for $AOA = 30^o$ due to the weakening of the wall suppression effect caused by the counterclockwise rotation of the cylinder.

2. *Clockwise rotation of the cylinder*

Figure 18$(a$-$c)$ shows the time-averaged drag coefficient ($\overline{C}_D$), the time-averaged horizontal component of the pressure force ($P_{x,f}$) acting on the front of the cylinder and the corresponding time-averaged horizontal force ($P_{x,b}$) acting on the backside of the cylinder for $G/D \in [0.6, 2.5]$ and $AOA = 0^o, -15^o, -30^o$ and -45^o at Re = 150. For $AOA = -15^o$, a general increase of $\overline{C}_D$ with increasing G/D is present due to the increase of $P_{x,b}$, as further visualized by $\overline{C}_p$ in figure 17(b). Moreover, a drag reduction is observed for $G/D \in [0.74, 0.8]$ due to the decrease of both $P_{x,f}$ and $P_{x,b}$. These behaviors are qualitatively similar to those observed for $AOA = 15^o$ (figure 16a-16c).

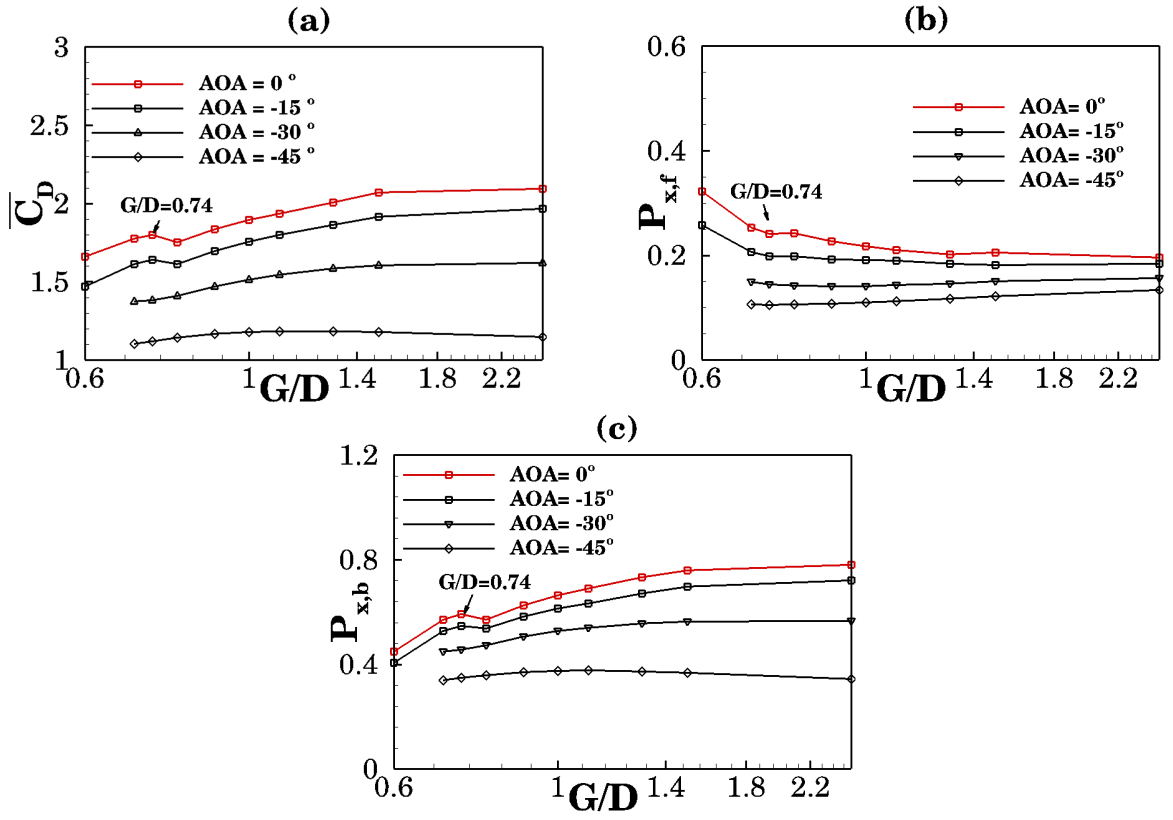

FIG. 18. Variation of (a) $\overline{C}_D$, (b) $P_{x,f}$ and (c) $P_{x,b}$ for flow around an elliptic cylinder with $AOA = -15^o, -30^o$ and -45^o near a moving wall for $G/D \in [0.6, 2.5]$ at $Re = 150$.

For $AOA = -30^o$, $\overline{C}_D$ increases as G/D increases, resulting from the combined effect of the nearly unchanged $P_{x,f}$ and the increase of $P_{x,b}$. Here $P_{x,f}$ is less affected by G/D than that observed for $AOA = 30^o$ (figure 16*b*) because the flow over the front of the cylinder for $AOA = -30^o$ is less affected by the moving wall. A qualitatively similar behavior is present for $AOA = -45^o$ but with a smaller $\overline{C}_D$, $P_{x,f}$, and $P_{x,b}$ for a given G/D than for $AOA = -30^o$ due to a decrease of the horizontal component of the pressure force acting on the cylinder.

Overall, the variation of $\overline{C}_D$ with G/D is qualitatively similar as that observed for the counter-clockwise rotation of the cylinder, with the same underpinning physical mechanisms. However, for a given G/D and for a given $|AOA|$, the value of $\overline{C}_D$ is larger for the counterclockwise rotated cylinder (figure 16*a*) than for the clockwise rotated cylinder (figure 18*a*). This might be due to two different physical mechanisms; *i*) for the clockwise rotated cylinder, the gap between the front of the cylinder and the moving wall results in stronger blockage effect than for the counterclockwise rotated cylinder, thus resulting in a stronger stagnation effect on the front of the cylinder, i.e., a larger $P_{x,f}$ for positive *AOA* (see figures 16*b* and 18*b*); *ii*) the vortex shedding behind the cylinder is less affected by the moving wall for the counterclockwise rotated cylinder than for the clockwise rotated cylinder, thus resulting in a larger $P_{x,b}$ for positive *AOA* (see figures 16*c* and 18*c*). Moreover, for a given G/D, an increase of $|AOA|$ (i.e., both clockwise and counterclockwise rotation) leads to a decrease of the horizontal component of the pressure force acting on the cylinder, i.e., a smaller $\overline{C}_D$, $P_{x,f}$, and $P_{x,b}$, except for $G/D \in [0.6, 1.0]$ where $\overline{C}_D$ is larger for $AOA = 15^o$ than for $AOA = 0^o$ (figure 16*a*). It appears that at small G/D, the stagnation effect at the front of the cylinder is stronger for $AOA = 15^o$ than for $AOA = 0^o$, counteracting the decrease of $P_{x,f}$ as the cylinder is rotated counterclockwise. The values of $P_{x,b}$ for $G/D < 0.9$ (figure 16*c*) remain nearly the same for $AOA = 0^o$ and 15^o due to the equilibrium between the decrease of $P_{x,b}$ caused by the rotation of the cylinder for $AOA = 15^o$ and the increase of $P_{x,b}$ due to the weaker wall suppression effect for $AOA = 15^o$.

D. Time-averaged lift coefficient, rms values of the lift coefficient and Strouhal number

Figure 19(a) shows the time-averaged lift coefficient ($\overline{C}_L$) for $G/D \in [0.6, 2.5]$ for $AOA = 0^o, \pm 15^o, \pm 30^o$ and $\pm 45^o$ at $Re = 150$. The results obtained from $AOA = 0^o$ by Zhu *et al.*[23] are included for comparison. For positive *AOA* (i.e., counterclockwise rotation of the cylinder), $\overline{C}_L$ decreases as G/D increases due to the weakening of the blockage effect at the gap, leading to more flow going through the gap. For negative *AOA* (i.e., clockwise rotation of the cylinder), the direction of the vertical component of the pressure force acting both on the backside and on the front of the cylinder is directed downwards, resulting in negative values of $\overline{C}_L$. Here $|\overline{C}_L|$ increases slightly as G/D increases due to a stronger vortex shedding with a resulting smaller pressure on the backside of the cylinder and thus a larger pressure difference between the backside and the front of the cylinder. Moreover, for a given G/D, $|\overline{C}_L|$ increases as $|AOA|$ increases due to an increase of the vertical component of the pressure force acting on the cylinder.

Figure 19(b) shows the rms values (root mean square) of the lift coefficient $C_L^{'} (= \sqrt{\frac{2}{N}\sum_{i=1}^{N}(C_{L,i} - \overline{C_L})^2})$ for $G/D \in [0.6, 2.5]$ for $AOA = 0^o, \pm 15^o, \pm 30^o$ and $\pm 45^o$ at $Re = 150$. For $AOA = 0^o$ and $\pm 15^o$, $C_L^{'}$ increases gradually as G/D increases while for $AOA = \pm 30^o$ and $\pm 45^o$, $C_L^{'}$ first increases

and then decreases slightly as G/D increases. Moreover, for a given G/D, $C_L^{'}$ remains nearly the same for $|AOA| \leq 15^o$. For $|AOA| = 30^o$, $C_L^{'}$ decreases for $G/D \geq 1.0$ due to the weakening of the interaction between vortices shed from the top and the bottom of the cylinder. However, for $G/D < 1.0$ and for $AOA = -30^o$, $C_L^{'}$ remains nearly the same as for $AOA = 0^o$ and $\pm 15^o$. This is because the wall suppression effect dominates, counteracting the effect of the rotation of the cylinder. It should be noted that for $AOA = 30^o$, $C_L^{'}$ is larger than for $AOA = -30^o$, and this difference appears to increase with decreasing G/D. This is because the counterclockwise rotation of the cylinder weakens the wall suppression effect. A qualitatively similar behavior is observed for $AOA = \pm 45^o$.

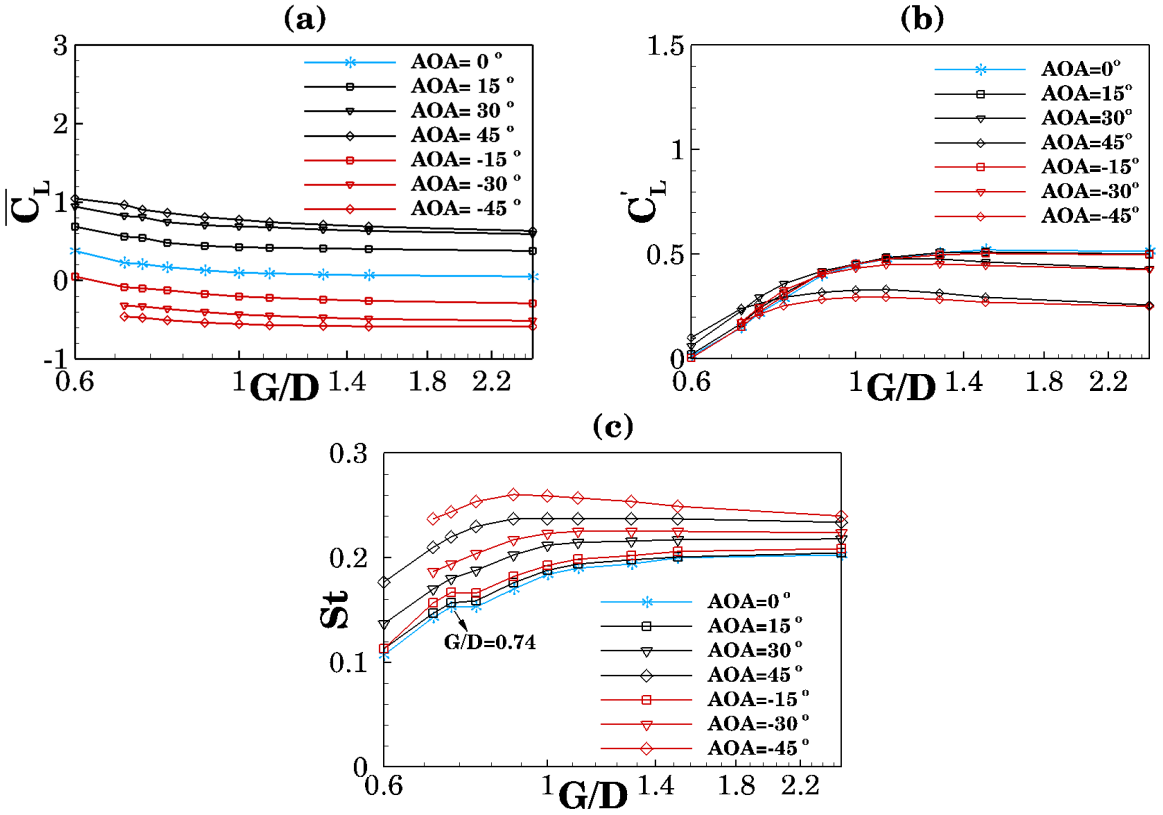

FIG. 19. (a) Time-averaged lift coefficient $\overline{C}_L$, (b) the root mean square of lift coefficient $C_L^{'}$ and (c) Strouhal number St for flow around the elliptic cylinder near a moving wall for $AOA = 0^o, \pm 15^o, \pm 30^o$ and $\pm 45^o$ and for $G/D \in [0.6, 2.5]$ at Re = 150.

Figure 19(c) shows the Strouhal number (St) for $AOA = 0^o, \pm 15^o, \pm 30^o$ and $\pm 45^o$ as well as for $G/D \in [0.6, 2.5]$ at $Re = 150$. The results for $AOA = 0^o$ obtained by Zhu *et al.*[23] are included for comparison. A general increase of St with increasing G/D (for a given AOA) is observed and is due to the weakening of the wall suppression effect. For $AOA = \pm 15^o$, St remains nearly constant for $G/D \in [0.74, 0.8]$, coinciding with the drag reduction of $\overline{C}_D$ shown in figures 16(a) and 18(a). Moreover, for $AOA = -45^o$, St decreases slightly as G/D increases from 1 to 2.5. This can be explained by that an increase of G/D leads to stronger vortices shed from the bottom part of the cylinder, enlarging the strength difference between the vortices shed from the top and the bottom part of the cylinder, resulting in a weaker interaction between the vortices (i.e., a smaller St).

As $|AOA|$ increases (for a given G/D) St increases,. This is qualitatively similar to the observation by, e.g., Paul, Arul Prakash, and Vengadesan[11] for flow over an isolated elliptic cylinder with different AOA. For a given $|AOA|$ (for a given G/D), St is larger for negative AOA than for positive AOA. This is because for negative AOA, the vortices shed from the top of the cylinder are weaker than the vortices shed from the bottom part of the cylinder while an opposite behavior is observed for positive AOA as shown in figures 5 and 15. Here the lower vortices are weakened by the wall suppression effect, thus resulting in a decrease and an increase of the strength difference between the upper and lower vortices for negative AOA and positive AOA, respectively. Consequently, the vortex interaction is stronger for negative AOA than for negative AOA, i.e., St is larger for positive AOA. Furthermore, the difference between St for positive and negative AOA increases as $|AOA|$ increases due to a larger strength difference between the upper and lower vortices.

VI. SUMMARY AND CONCLUSIONS

In the present work, the flow around an elliptic cylinder, which is either clockwise (negative angle of attack AOA) or counterclockwise (positive AOA) rotated relative to the normal direction from the moving bottom wall, is investigated. Here AOA ranges from -45^o to 45^o, the gap ratio G/D (where G denotes the distance between the cylinder center and the moving wall) ranges from 0.6 to 2.5, and the Reynolds number is 150 based on the semi-major axis length of the cylinder and the free-stream velocity. The aspect ratio of the cylinder is fixed to 0.4. The resulting wake patterns, vortex shedding, the drag and lift coefficients as well as the Strouhal number (St) have been investigated and discussed in details. The main results from this work can be summarized as follows:

- The rotation of the cylinder leads to a strength difference between the vortices shed from the top and bottom part of the cylinder. Thus, the parameter range of the four wake patterns previously presented in Zhu *et al.*[23] for flow over a non-rotated elliptic cylinder near a moving wall, now depends both on the gap ratio and the angle of attack. These four wake patterns have been mapped out in (G/D, AOA)-space.

- For small gap ratios, the clockwise rotation of the cylinder leads to a stronger wall suppression effect than for the counterclockwise rotation, since the clockwise rotation results in a smaller gap between the backside of the cylinder and the moving wall. Consequently, for $G/D = 0.6$, the steady wake pattern (where vortex shedding is absent) only occurs for the clockwise rotated cylinder.

- The rotation of the cylinder leads to a decrease of the horizontal component of the pressure force acting on the cylinder, which again leads to a decrease of the time-averaged drag coefficient relative to that for the non-rotated cylinder. However, for $G/D \leq 0.9$, a counterclockwise rotation from 0^o to 15^o leads to an increase of the time-averaged drag coefficient. This is caused by an increase of the pressure force acting on the front of the cylinder due to a blockage effect in the gap between the front of the cylinder and the moving wall.

- For the counterclockwise rotated cylinder, the time-averaged lift force is directed upwards and decreases with increasing G/D due to the decrease of the pressure force acting on the

cylinder front. For the clockwise rotated cylinder, the time-averaged lift force is directed downwards, and its magnitude increases with increasing G/D due to the weakening of the wall suppression effect on the vortex shedding behind the cylinder.

- The rotation of the cylinder leads to a shorter vortex shedding period, i.e., an increase of the Strouhal number St. Furthermore, the clockwise rotation of the cylinder weakens the upper vortices, whilst the resulting wall supression weakens the lower vortices. For the counterclockwise rotation of the cylinder, however, the lower vortices are more weakened (due to the wall supression) than for the clockwise rotation, while the upper vortices are strengthened. Consequently, the strength difference between the upper and lower vortices is smaller for the clockwise rotated cylinder than for the counterclockwise rotated cylinder. Thus, a stronger vortex interaction, i.e., a larger St, is observed for the clockwise rotated cylinder.

ACKNOWLEDGEMENTS

We gratefully acknowledge the support for this research from the Department of Marine Technology, Norwegian University of Science and Technology and the Norwegian Research Council, Grant number 308745.

DATA AVAILABILITY

The data that support the findings of this study are available from the corresponding author upon reasonable request.

REFERENCES

[1]M. M. Zdravkovich, *Flow Around Circular Cylinders—Volume 1: Fundamentals* (Oxford University Press, 1997).
[2]B. M. Sumer *et al.*, *Hydrodynamics around cylindrical strucures*, Vol. 26 (World scientific, 2006).
[3]J. M. Cimbala, H. M. Nagib, and A. Roshko, "Large structure in the far wakes of two-dimensional bluff bodies," Journal of Fluid Mechanics **190**, 265–298 (1988).
[4]W. W. Durgin and S. K. Karlsson, "On the phenomenon of vortex street breakdown," Journal of Fluid Mechanics **48**, 507–527 (1971).
[5]T. Karasudani and M. Funakoshi, "Evolution of a vortex street in the far wake of a cylinder," Fluid Dynamics Research **14**, 331 (1994).
[6]B. Kumar and S. Mittal, "On the origin of the secondary vortex street," Journal of Fluid Mechanics **711**, 641–666 (2012).
[7]R. Mittal and S. Balachandar, "Direct numerical simulation of flow past elliptic cylinders," Journal of Computational Physics **124**, 351–367 (1996).
[8]B. Jensen, S. Carstensen, and E. Christensen, "Mixing of stratified flow around bridge piers in steady current," Journal of Hydraulic Engineering **144**, 04018041 (2018).

[9]W. Khan, J. Culham, and M. M. Y., "Fluid flow around and heat transfer from elliptical cylinders: analytical approach," Journal of Thermophysics and Heat Transfer **19**, 178–185 (2005).
[10]M. Thompson, A. Radi, A. Rao, J. Sheridan, and K. Hourigan, "Low-Reynolds-number wakes of elliptical cylinders: from the circular cylinder to the normal flat plate," Journal of Fluid Mechanics **751**, 570 (2014).
[11]I. Paul, K. Arul Prakash, and S. Vengadesan, "Numerical analysis of laminar fluid flow characteristics past an elliptic cylinder: A parametric study," International Journal of Numerical Methods for Heat & Fluid Flow **24**, 1570–1594 (2014).
[12]X. Shi, M. Alam, and H. Bai, "Wakes of elliptical cylinders at low Reynolds number," International Journal of Heat and Fluid Flow **82**, 108553 (2020).
[13]S. Taneda, "Experimental investigation of vortex streets," Journal of the Physical Society of Japan **20**, 1714–1721 (1965).
[14]M. Zdravkovich, "Observation of vortex shedding behind a towed circular cylinder near a wall," in *Flow Visualization III* (1985) pp. 423–427.
[15]T. Nishino, G. T. Roberts, and X. Zhang, "Vortex shedding from a circular cylinder near a moving ground," Physics of Fluids **19**, 025103 (2007).
[16]W. Huang and H. Sung, "Vortex shedding from a circular cylinder near a moving wall," Journal of Fluids and Structures **23**, 1064–1076 (2007).
[17]A. Rao, M. C. Thompson, T. Leweke, and K. Hourigan, "The flow past a circular cylinder translating at different heights above a wall," Journal of Fluids and Structures **41**, 9–21 (2013).
[18]H. Jiang, L. Cheng, S. Draper, and H. An, "Two- and three-dimensional instabilities in the wake of a circular cylinder near a moving wall," Journal of Fluid Mechanics **812**, 435–462 (2017).
[19]I. C. Rust and H. H. Asada, "The eyeball ROV: Design and control of a spherical underwater vehicle steered by an internal eccentric mass," in *2011 IEEE International Conference on Robotics and Automation* (IEEE, 2011) pp. 5855–5862.
[20]A. Mazumdar, M. Y. Chuah, M. S. Triantafyllou, and H. H. Asada, "Design for precision multi-directional maneuverability: Egg-shaped underwater robots for infrastructure inspection," in *2014 IEEE International Conference on Robotics and Automation (ICRA)* (IEEE, 2014) pp. 2950–2956.
[21]A. Zarghami and J. T. Padding, "Drag, lift and torque acting on a two-dimensional non-spherical particle near a wall," Advanced Powder Technology **29**, 1507–1517 (2018).
[22]H. R. Beem and M. S. Triantafyllou, "Wake-induced 'slaloming'response explains exquisite sensitivity of seal whisker-like sensors," Journal of Fluid Mechanics **783**, 306–322 (2015).
[23]J. Zhu, L. E. Holmedal, D. Myrhaug, and H. Wang, "Near-wall effect on flow around an elliptic cylinder translating above a plane wall," Physics of Fluids **32**, 093607 (2020).
[24]J. Zhu and L. E. Holmedal, "A numerical study of separation and stagnation points for steady and unsteady flow over an elliptic cylinder near a moving wall," Physics of Fluids **33**, 083617 (2021).
[25]F. M. White and J. Majdalani, *Viscous fluid flow*, Vol. 3 (McGraw-Hill New York, 2006).